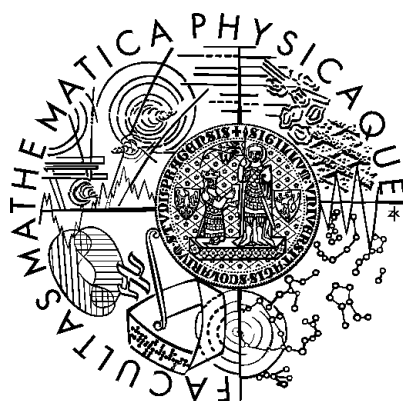


CHARLES UNIVERSITY IN PRAGUE
FACULTY OF MATHEMATICS AND PHYSICS

Diploma Thesis



ALEXANDER KUTKA

Lucky Imaging for RTS

Department of Software and Computer Science Education

Supervisor: Prof. Ing. Jan Flusser, DrSc.

Study branch: Computer Science

Acknowledgments:

I would like to thank the supervisor of this work, prof. Jan Flusser, for his advices and comments, and for lending software-fragments used in this work. I also would like to express great thank to Mgr. Petr Kubánek, the consultant of this work, for his numerous advices and tips, and for his willingness and encouragement.

This research made use of Montage, funded by the National Aeronautics and Space Administration's Earth Science Technology Office, Computation Technologies Project, under Cooperative Agreement Number NCC5-626 between NASA and the California Institute of Technology. Montage is maintained by the NASA/IPAC Infrared Science Archive.

I declare that I wrote the master thesis on my own, using only the referenced sources. I approve lending of this thesis.

Prague, August 10th 2007

Alexander Kutka

Contents

1	Introduction	6
1.1	Scintillation	6
1.2	Possible solutions	7
1.2.1	Space-based telescopes	7
1.2.2	Adaptive optics	7
1.2.3	Lucky imaging	8
1.3	Thesis structure	10
2	Problem formulation and goals	11
3	Astrophotographic fundamentals	12
3.1	Image acquisition	12
3.2	Point spread function	14
4	Focus measures – a review	15
4.1	Traditional focus measures	16
4.2	Recent focus measures	17
4.2.1	Moments measure	17
4.2.2	Wavelet measure	19
5	Strehl ratio – a focus measure for star images	20
5.1	Star detection – the Kappa-sigma clipping algorithm	21
5.2	Star centroid computation	22
5.3	Star flux computation	23
5.4	Strehl ratio computation	24
6	Image registration	26
6.1	World Coordinate System	27
6.2	Registration of images of stars	29
6.2.1	Image re-projection	29
6.2.2	Common background estimation	31
6.2.3	Image composition	31
6.3	Registration of planetary images	32

6.3.1	Correlation	32
6.3.2	Cross-correlation registration	33
7	Experiments and tests	35
7.1	Experimental part	35
7.1.1	Artificial blurring	36
7.1.2	Defocustion	42
7.2	Tests on real data	47
7.2.1	Lucky imaging of ζ -Bootis	48
7.2.2	Lucky imaging of Saturn	51
7.3	Conclusion of tests and experiments	55
8	Conclusion and further improvements	56
A	The LI-software	57
A.1	User documentation	57
A.2	CD content	58
B	Used telescope, CCD and software environment	59
B.1	RTS2	59
B.2	Bootes-IR	59
B.3	Watcher	60

Název práce: Lucky Imaging for RTS2

Autor: Alexander Kutka

Katedra: Kabinet software a výuky informatiky

Vedoucí diplomové práce: Prof. Ing. Jan Flusser, DrSc.

E-mail vedoucího: flusser@utia.cas.cz

Abstrakt:

S rychlým vývojem CCD detektorů se v astronomii v posledních několika letech začíná používat metoda zvaná Lucky Imaging. Ta, podobně jako adaptivní optika, umožňuje pořizování snímků s rozlišením blízkému difrakčnímu limitu, tedy umožňuje pozemskými přístroji pořizovat obrázky, které mají rozlišení podobné přístrojům umístěným mimo atmosféru. Ve srovnání s adaptivní optikou bývá Lucky Imaging levnější a méně náročný na přítomnost referenčních hvězd.

Diplomová práce je implementace Lucky Imagingu do softwarového systému pro řízení pozorování RTS2. Podrobně jsou studovány tři algoritmy pro vyhodnocování ostrosti snímků a jejich výkon je porovnán na snímcích pořízených astronomickým dalekohledem. V druhé části práce jsou studovány dvě metody snímkové registrace, které jsou v práci použity pro potlačení šumu na obrázcích.

Klíčová slova: Lucky imaging, Měření ostrosti, Registrace obrázků

Title: Lucky Imaging for RTS2

Author: Alexander Kutka

Department: Department of Software and Computer Science Education

Supervisor: Prof. Ing. Jan Flusser, DrSc.

Supervisor's e-mail address: flusser@utia.cas.cz

Abstract:

Thanks to the rapid development of CCD detectors there is a method called "Lucky Imaging" being used in astronomy in the past years. Like adaptive optics, Lucky imaging makes it possible to gain pictures with resolution close to the diffraction limit, i.e. it gives to ground based telescopes the possibility to gain pictures with the resolution close to the resolution of telescopes placed outside the atmosphere. Lucky imaging is cheaper alternative to Adaptive Optics, with a lower demandingness on the presence of reference stars.

This Diploma thesis is an implementation of Lucky Imaging into a software system for robotics observatory control called "RTS2". Three algorithms for evaluation of image focus are studied and their performance is compared on digital images acquired by a telescope. In the second part of the thesis, two methods of image registration are studied, which are used to suppress noise on the acquired images.

Keywords: Lucky imaging, Focus measure, Image registration

Chapter 1

Introduction

Astrophotography¹ is a common method of studying the universe. Although professional astronomers make use of the whole spectrum of electromagnetic radiation of space objects, ranging from radio-waves to γ -rays, observations in the visible light are most often in astronomy.

The thesis theme – Lucky imaging – is a particular method of increasing the quality of astrophotographic images. More precisely, the angular resolution of these images are improved, i.e. the ability to distinguish two point light-sources lying angular close to each other. In this chapter, the reasons for degradation of this angular resolution will be presented, as well as another well-known methods of enhancing it, namely space-based telescopes and Adaptive Optics.

1.1 Scintillation

Ground based observations suffer of one fundamental fact – the Earth is surrounded by its atmosphere, which is almost permanently under motion. Mixing of cold and warm air causes air turbulations of various intensity. The atmosphere can therefore be considered to be an optical environment of time-varying refractive index. Individual light rays passing such an unhomogenous environment are each bend into slightly different directions; the wrapping wavefront of those light-rays is therefore perturbed (see Fig. 1.1). When observing a light-source through such an unstable environment, it seems to change rapidly its brightness and/or color. This phenomenon is called the *scintillation effect* of the atmosphere. Sometimes this scintillation, or “twinkling” of stars is also observable by an unweaponed eye.

Scintillation is a serious problem for astronomical observations, as it causes two close light-sources to blur into one single blot, and limits therefore

¹Photography of astronomical objects in the wavelength cca. $400\mu\text{m}$ (violet color) – $700\mu\text{m}$ (red color).

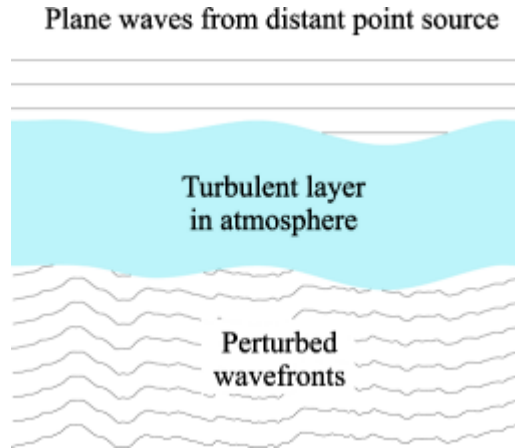


Figure 1.1: Perturbation of wavefront due to turbulent atmosphere, [30].

the angular resolution of ground-based telescopes. The theoretical maximum of the angular resolution, called the *diffraction limit*, is, as stated in [1], proportional to λ/D , where λ is the wavelength of the observed light and D the telescope’s aperture diameter. However, due to scintillation, angular resolution of telescopes with apertures larger than 10 cm are all approximately at 0.4 arcseconds, [1]. Without a solution of this problem, it would not make sense to build telescopes having $D > 10$ cm.

1.2 Possible solutions

1.2.1 Space-based telescopes

A straight-forward solution of the resolution limitation caused by scintillation is simply to place the telescope outside the atmosphere. That is indeed the case of, for example, the *Hubble Space Telescope* (HST), which flies on the Earth’s orbit since April 1990. Unfortunately, such a solution has many disadvantages: reparations or break-downs are problematic due to difficult accessibility. Also the size of the instrument is limited (for example, the HST’s primary mirror is only 2.4 m in diameter, due to the load capacity and size of the Space Shuttle’s cargo bay). The costliness of such a solution is also very considerable.

1.2.2 Adaptive optics

A much more rife approach, called “Adaptive optics” (see [1]), is based on the idea of compensation of the scintillation effect, rather than avoiding it. In this case, a small deformable mirror is put into the optical path of the

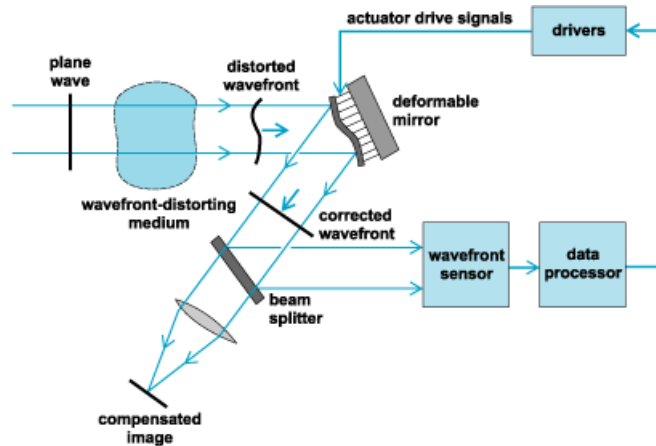


Figure 1.2: The scheme of the adaptive optics system, [31]

telescope² and is meant to have such a shape, that the actual wavefront distortion is cancelled (see Fig. 1.2). For that purpose, a bright reference star is co-observed and its image analyzed by a wavefront sensor. Based on this analysis the optimal shape of the deformable mirror is computed and the mirror appropriately deformed. These reshape happens for several hundred times a second (~ 100 Hz).

“Adaptive optics” is not to be confused with “Active optics”, which is a different system, designed for shape corrections of the primary mirror itself. Because the primary mirror is usually very thin (and therefore can be made large), even small wind or minor gravitational changes can cause significant unwanted mirror deformations. Active optics measures these deformations and with a set of actuators keeps the mirror in optimal shape. These reshapes happen in the order of seconds (~ 1 Hz), rather than $\frac{1}{100}$ of seconds, as it is in the case of Adaptive optics.

1.2.3 Lucky imaging

Lucky Imaging (LI) is the technique discussed in this thesis. It is a software approach in the problem of angular resolution enhancement. LI makes use of fast-working CCD’s able to obtain a shot several times a second, and relies on the possibility, that among all the pictures taken, some of them might be well-focused because the actual wavefront distortion was minimal, none or even has been cancelling imperfections of the telescope (i.e. the wavefront distortion caused by the atmosphere was inverse to the wavefront distortion caused by the imperfections of the telescope’s optical system). After hundreds of short-exposed photographs of the same object have been

²Recently, adaptive optics has been used on the secondary mirror directly, [2].

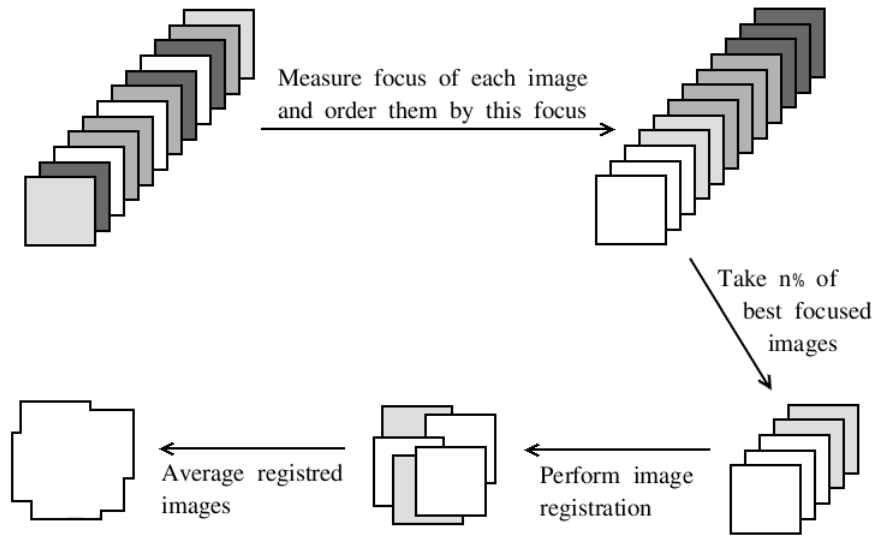


Figure 1.3: Lucky imaging: focus of each image is evaluated and best focused images are assembled into one final image (for better imagination, the gray level of an input image indicates its focus).

taken, they are searched for the well-focused ones. For this purpose a *focus-measure* is used – a function, which expresses the focus of an image as a number.

As will be explained later, short exposed astronomical images contain fairly strong noise. One of the best-known denoising techniques is to average more images of the same scene (see [3] for further details) – well-focused images selected by the appropriate focus-measure are therefore combined into a single one, by a process called *image registration*. It is a process of finding the proper space matching (e.g. rotation, translation) of the input images and a suitable averaging of their pixel-values.

A scheme of the entire LI-process is shown on figure 1.3: input images are measured on focus, n% of best images are taken, registered and averaged into a final output image.

Objects of interest, which astronomers want to photograph, are mostly very faint and are visible only on long-exposed images, when the little light emitted by the object is integrated over many minutes (or even hours). Averaging of images in the image registration process has the same effect as long exposures in classical astrophotography, with the difference, that because only undistorted, unblurred images are averaged, the final image shows fainter objects in a better focus.

LI represents a cheaper alternative to the traditional Adaptive Optics (AO) technique, since it is a pure software solution, and makes no demands on any special hardware. On the other hand, since many time-consuming

computation have to be done (mainly during image registration), LI is a slower solution to the hardware-based AO system.

A significant work on Lucky Imaging has been done by professional astronomers grouped in the Lucky Imaging Team at University of Cambridge, UK, [4]. The authors achieved valuable resolution enhancement, achieving at good observational conditions diffraction limited images. Another works concerning Lucky Imaging are listed on the team website, [5].

1.3 Thesis structure

This thesis is divided into 8 chapters and 2 appendices. The second chapter sets the direct goals of this thesis. The third chapter characterizes the processed data. The fourth chapter is a review of several known planar focus-measures, three of them which are used in this work. The fifth chapter introduces a special focus-measure designed extra for astronomical images. The sixth chapter describes two registration techniques used in this work. The seventh chapter summarizes practical experiments and tests done within this work. The eighth chapter concludes this thesis and raises future works proposals.

Appendix A is the documentation of the produced software. Appendix B contains technical information about the instruments used to acquire the processed data (telescopes and camera) and a characterization of the RTS system used to control the observations and into which the produced software can be integrated.

Chapter 2

Problem formulation and goals

As described in section 1.2.3, Lucky Imaging consist of two separate parts: focus-measuring and image registration.

The first goal for this thesis is therefore to find a suitable focus-measure technique for astronomical images – photographs of stars, which are considered to be point light-sources, as well as for planetary shots, which are in contrast areal objects and therefore show properties different from images of stars.

A good focus-measure should have high discriminability, i.e. it should distinguish well between focused and unfocused images, and it should be monotonic, i.e. it should descend with increasing blur. It should also be robust to noise, i.e. its discriminability should not be too affected by increasing amount of noise.

The second goal of this thesis is to review image-registration techniques and use a proper one to assemble previously chosen well-focused images into a final image of higher angular resolution and suppressed noise.

The applicability of the whole software should be demonstrated on real data. The computation speed of the software is not a priority, as the system will be used as a post-processing tool.

Chapter 3

Astrophotographic fundamentals

This chapter introduces the character of processed data, since astronomical images differ in many ways from common scene images.

The definition of a digital image is well-known and can be found in many papers and books concerning digital image processing (e.g. [6]). For convenience it is reminded, that a digital image g is considered to be a two-dimensional array of $N \times M$ integer pixels g_{ij} representing the brightness-level in the sensed area:

$$g := \{g_{ij}\}_{1 \leq i \leq N; 1 \leq j \leq M}$$

where N is the count of rows and M the count of columns of the array.

In this work, however, an image g is referred as a function $g(i, j)$, rather than a set $\{g_{ij}\}$, whereas in some moments there is more suitable to speak about a *continuous* function g (defined to zero outside the image borders), while in other moments rather about a *discrete* one. This duality is acceptable, as the discrete function is only a sampled version of the continuous one. For more details on sampling, see [6].

3.1 Image acquisition

Today, digital images of all kind are obtained by a so called *Charged-couple device* (CCD) camera, invented in 1970's (see [7]) and developed till today. In principle, it is a two-dimensional array of light-sensible units, converting impinging photons of light into electrical impulses thanks to a physical phenomenon known as the "photoeffect". This per-pixel analog signal is then converted to a digital one by an A/D converter, and the resulting image is read out.

Before the invention of the CCD, astrophotography was made on photographic plates, i.e. glass planes covered with photosensitive emulsions. This

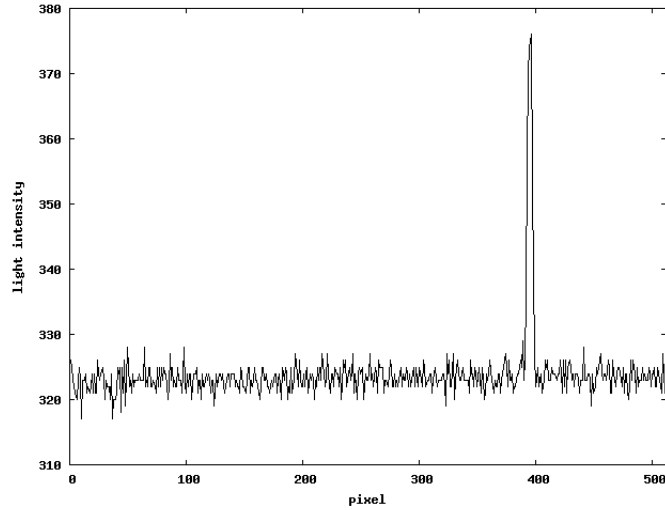


Figure 3.1: A typical row-profile of a star in a digital image. The star peak rises above the noisy background.

classical technique, which was in use since the 19th century, has been gradually replaced by digital astrophotography making use of CCD's since the 1990's.

As it has been mentioned earlier, digital astronomical images contain fairly strong white noise (which is a well known sort of noise, see e.g. [6]). Not only the internal electronic of a CCD products noise¹, also the sky itself is noisy; sunlight reflected by the Moon, the Earth itself and the dust particles spread out over the Solar system, light contributions of other undistinguishable stars and galaxies and even urban light pollution – all this contributes to a noisy background of digital astronomical pictures.

A row profile of a typical astronomical image of a star is shown in Fig. 3.1. As can be seen, the star, although considered to be a point source of light, is not sensed as a single high value in the CCD-array. Instead, a narrow Gaussian "hat" is rendered. More precisely, the image of a star can be well approximated by a normal distribution function N of standard deviation σ :

$$N_{\sigma}(x, y) = \frac{c}{\sqrt{2\pi}\sigma} e^{-\frac{x^2+y^2}{2\sigma^2}} \quad (3.1)$$

where c is a scaling constant.

The reasons for this way of star-rendering will be explained in the following section.

¹See [8] for further details on so-called Read noise, Dark noise and Shot noise of a CCD camera.

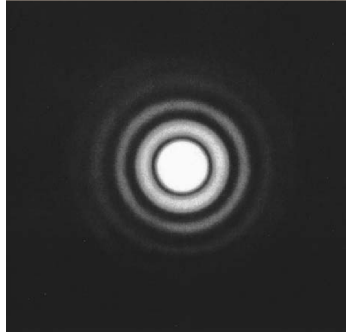


Figure 3.2: The Airy disc - the diffraction pattern of a round aperture, [27].

3.2 Point spread function

In fact, not only point light-sources are blurred over a small area – also areal objects are blurred in a certain amount. Every optical system shows this degradation of the imaged scene – even the human eye. This degradation is mostly expressed as the *Point Spread Function* (PSF) of the imaging optical system. A PSF of a system is a characterization of its quality – it shows, how focused is a point light-source imaged in the focal plane of the system.

Mathematically expressed, the resulting image g is a convolution of the original scene f and the optical system’s PSF h :

$$g = f * h \tag{3.2}$$

There are two main reasons, why every optical system blurs imaged objects with a certain PSF. The first one is that light, due to its wave-nature, diffracts on the aperture of the imaging system (i.e. the tubus of a telescope, the pupilla of the eye, etc.). As stated in [9], the resulting image of a single point light-source is a Fourier transformation of the aperture’s shape – in the case of the circular aperture of a telescope, this pattern is called the *Airy disc* (see Figure 3.2).

The Airy disc represents a PSF of an ideal imaging system, i.e. with no imperfections or defects. However, practically every system shows some imperfections, called “aberrations”, such as spherical and/or chromatic aberrations of its pupils, aberrations of the mirror shapes, etc. These aberrations contribute to the shape of the PSF, therefore the final PSF is a combination of the Airy disc and the aberration. Because the side lobes of the Airy disc are negligible, and all other aberrations are of stochastic nature, the final PSF has a shape of a Gaussian normal distribution (see Eq. 3.1). Therefore stars, considered to be single point light-sources, are rendered in the shape of this distribution.

Chapter 4

Focus measures – a review

In this chapter a review of chosen existing focus measures will be given¹, namely the Gray level variance, the Energy of image gradient, the Energy of Laplacian, a measure based on central moments of the image and a measure based on the wavelet decomposition.

Unfortunately, none of these measures is suitable for measuring blur in images of stars, as they have been developed for measuring focus on areal objects, which cannot be found in an image composed of Gaussian profiles. Therefore, a specially developed focus-measure will be used for images of stars, namely the *Strehl ratio* measure, described in chapter 5.

On the other hand, focus measures described in this chapter have been successfully used in this work for measuring focus on planetary images, since planets are areal objects, good distinguishable from the background. Their effectiveness on planetary images is evaluated in chapter 7.

A good focus measure should satisfy following requirements ([10]):

1. independence of image content
2. monotonicity with respect to blur (e.g. to standard deviation of the function convolving the original scene) – this requirement, however, is hard to achieve in general
3. large variation in value with respect to the degree of blurring
4. minimal computation complexity
5. robustness to noise

¹For a more exhausting review, see [10].

4.1 Traditional focus measures

Measuring focus of images is not a new idea. It was firstly studied by M. Subbarao in 1992 (see [11]), for purposes of automatic camera focusing. Subbarao proposed several basal focus-measuring techniques, which are based on the idea of emphasizing high frequencies of the image and measuring their quantity.

Each of the following measures is expressed in its analytical² and discrete form:

1. Gray level variance

Analytical form:

$$M_1 := \int \int (g(x, y) - \mu)^2 dx dy$$

Discrete form:

$$M_1 := \sum_i \sum_j (g(i, j) - \mu)^2$$

where μ denotes the mean gray level value of image g . Subbarao proved this measure to be monotonic (with respect to increasing blur) and, for zero-mean images, equivalent to the image energy in Fourier domain.

2. Energy of image gradient

Analytical form:

$$M_2 := \int \int \left(\frac{\partial g(x, y)}{\partial x} \right)^2 + \left(\frac{\partial g(x, y)}{\partial y} \right)^2 dx dy$$

Discrete form:

$$M_2 := \sum_i \sum_j (g_i^2 + g_j^2)$$

where

$$g_i := g(i + 1, j) - g(i, j)$$

$$g_j := g(i, j + 1) - g(i, j)$$

²Analytical formulas suppose a continuous image $g(x, y)$.

3. Energy of Laplacian of the image

Analytical form:

$$M_3 := \int \int \left(\frac{\partial^2 g(x, y)}{\partial x^2} + \frac{\partial^2 g(x, y)}{\partial y^2} \right)^2 dx dy$$

Discrete form:

$$M_3 := \sum_i \sum_j (g_{ii} + g_{jj})$$

where

$$\begin{aligned} g_{ii} + g_{jj} := & -g(i-1, j-1) - 4g(i-1, j) - g(i-1, j+1) \\ & -4g(i, j-1) + 20g(i, j) - 4g(i, j+1) \\ & -g(i+1, j-1) - 4g(i+1, j) - g(i+1, j+1) \end{aligned}$$

Subbarao proved also M_2 and M_3 to be monotonic, and showed that both measures can be equivalently evaluated in Fourier domain as the energy of high-pass filtered image ([12]).

4.2 Recent focus measures

In the first years of the 21st century, two new techniques for measuring focus in images appeared. The first one was proposed by Zhang et al., 2000 ([13]), based on central moments of the image. The second one was proposed by Flusser et al., 2002 ([12]), based on wavelet decomposition of the image. Both of these measures have been used in this work for evaluating focus of planetary images. The test results and the comparison with the traditional M_1 gray level variance measure can be found in chapter 7.

4.2.1 Moments measure

A *central moment* μ_{pq} of a *continuous* image $g(x, y)$, where p, q are non-negative integers and $(p + q)$ is called the *order* of the moment, is defined as follows ([14]):

$$\mu_{pq}^{(g)} = \int_{-\infty}^{\infty} \int_{-\infty}^{\infty} (x - x_c^{(g)})^p (y - y_c^{(g)})^q g(x, y) dx dy$$

where the coordinates $(x_c^{(g)}, y_c^{(g)})$ denote the centroid of the continuous image $g(x, y)$:

$$x_c^{(g)} := \frac{\int_{-\infty}^{\infty} \int_{-\infty}^{\infty} x \cdot g(x, y)}{\int_{-\infty}^{\infty} \int_{-\infty}^{\infty} g(x, y)} \quad (4.1)$$

similar for y .

The proposed measure is based on the theoretical results of Flusser and Suk, who have shown, as stated in [12], that even-order moments change under blur (while odd-order moments are blur-invariant).

As it has been stated in section 3.2 Eq. 3.2, an image g might be expressed as a convolution of the original scene f and the PSF h of the image-acquiring system:

$$g = f * h$$

where h is “energy preserving”, i.e.

$$\int_{-\infty}^{\infty} \int_{-\infty}^{\infty} h(x, y) dx dy = 1. \quad (4.2)$$

Considering the relationship of the central moments of g , f and h (see Eq. (3.7) in [13])

$$\mu_{pq}^{(g)} = \sum_{k=0}^p \sum_{l=0}^q \binom{p}{k} \binom{q}{l} \mu_{k,l}^{(h)} \mu_{p-k,q-l}^{(f)},$$

the central moment $\mu_{20}^{(g)}$ of the image g can be expressed as

$$M_4 := \mu_{20}^{(g)} = \mu_{20}^{(f)} + \mu_{00}^{(f)} \mu_{20}^{(h)}$$

since $\mu_{00}^{(h)} = 1$ (see Eq. (4.2)). Since $\mu_{20}^{(f)}$ and $\mu_{00}^{(f)}$ are always the same for each g , M_4 is indeed a measure of the blur h convolving the original scene.

Unfortunately, this method has one strong limitation – it can be shown ([13]), that the boundary effect (i.e. artificial edges on the image border, when periodically extended) strongly deteriorates the monotonicity of this measure. However, on zero-background (or constant-background) images this measure performs well. Therefore, in this work images have been thresholded by an appropriate value (e.g. by value 2μ , where μ is the mean of the image), before applying the moments-measure on them.

Note, that M_4 is a blur-measure (i.e. grows with blur), rather than a focus-measure (i.e. descends with growing blur). Well-focused images are therefore found under those with the lowest M_4 evaluation.

The blur measure used in this work was finally the expression

$$\frac{\mu_{20}^{(g)} + \mu_{02}^{(g)}}{\mu_{00}^{(g)}},$$

i.e. it was normalized by the total sum of g . The MATLAB[®]-code for this measure was kindly lend by prof. Flusser, the supervisor of this Master thesis.

4.2.2 Wavelet measure

As it has been mentioned before, the wavelet focus measure was proposed by Flusser et al. in 2002 ([12]), making use of the Discrete wavelet transform (DWT) of the processed image. DWT is exhaustingly described in the book [15]; however, for understanding of the measure being described it is important to know, that DWT examines contributions of certain frequency bands at a certain location on the image. The result of a DWT of an image is a set of coefficients expressing which frequency bands generates which areas of the image³, roughly speaking.

The resulting DWT-coefficients can be divided into a low-pass band $l_w(g)$ and several high-pass bands, collectively denoted as $h_w(g)$, where w denotes the used mother wavelet and g the decomposed image. In this implementation, the Daubechies D4 wavelet transform was used (see e.g. [16]), with the decomposition depth equal to 4, which means that one low-pass band and 12 high-pass bands are produced per image.

The used wavelet focus measure is then a measure of the high-pass bands, divided by the measure of the low-pass band:

$$M_5 := \frac{\|h_w(g)\|}{\|l_w(g)\|}$$

where the norm $\|\cdot\|$ is the traditional Euclidean norm, i.e. $\|f\| := \sqrt{\sum_i f(i)^2}$.

The argument, why should M_5 be a measure of focus, is, that the high-pass bands $h_w(g)$ contain large coefficients only where the image is focused (and will therefore increase the value of M_5), while smooth areas of the processed image contribute to higher coefficients in the low-pass band $l_w(g)$ (and will decrease the value of M_5).

The MATLAB[®]-code for the wavelet focus measure was again kindly lend by prof. Flusser.

³Therefore, DWT can be understood as a sort of generalization of the classic Fourier transform (FT), as FT examines concrete frequencies generating the whole image.

Chapter 5

Strehl ratio – a focus measure for star images

This chapter introduces a focus measure designed for astronomical images containing only stars. As it has been stated in section 3.1, stars are rendered as Gaussian “hats” (see Fig. 3.1) – therefore, the focus of such images cannot be measured by traditional approaches (listed in chapter 4), which rely on edge appearance in the processed images. Instead, a new focus-measure must be found, which makes use of the Gaussian profiles present in the image.

The *Strehl ratio*¹ is such a measure. It is based on the idea, that on well-focused images, stars are rendered as narrow spikes, while on blurred images, the rendered Gaussian profile is “wider”, i.e. it has a larger support (in a redefined manner, since the support of a regular Gaussian distribution is the whole real axis). The Strehl ratio is then, roughly speaking, computed as a ratio of the sensed Gaussian profile and a pre-computed ideal profile (i.e. the PSF of the telescope, see 3.2). This ratio is therefore always in the range $(0, 1)$.

Before giving the exact definition of the Strehl ratio and the description of the algorithm for computing it, three auxiliary algorithms have to be introduced: the “Kappa-sigma algorithm” (section 5.1) used for star detection, the star centroid computation algorithm (section 5.2), and the star flux computation algorithm (section 5.3).

The overall work-flow of the strehl-computation algorithm can be seen in section 5.4.

¹Firstly described by Karl Strehl (1864 – 1940), see [17].

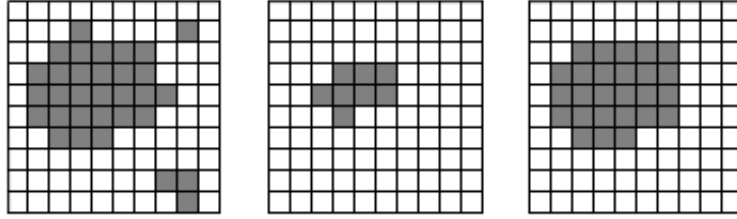


Figure 5.1: Morphological erosion and dilatation: the binary images M , M_e and M_d .

5.1 Star detection – the Kappa-sigma clipping algorithm

The *Kappa-sigma clipping algorithm* (KS) segments individual stars in the input image. More precisely: The input of the algorithm is a digital image g of size $N \times M$ and a real threshold parameter κ (in this implementation set to the value 5). The output is a set of “blobs”, i.e. sets of pixels $\beta \subset g$, together with their centroids $[i_\beta, j_\beta]$. Each blob β represents an estimation of a star area, while the centroid $[i_\beta, j_\beta]$ of a blob β represents the first (and rough) estimation of the star center, which will be later used to compute a more precise star-center estimation.

The KS algorithm works as follows:

1. $\mu :=$ median value of g
2. $\sigma := \frac{1}{NM} \sum_{i=1}^N \sum_{j=1}^M |g(i, j) - \mu|$
3. Create a binary image M of the image g , by thresholding it with the value $\kappa \cdot \sigma^2$:

$$M(i, j) := \begin{cases} 1 & \text{if } g(i, j) > \kappa \cdot \sigma \\ 0 & \text{otherwise} \end{cases}$$

4. Perform a morphological erosion and dilatation on image M to close all regions smaller than 3×3 and to cut off little salient pixels at the edges of the blobs (see Fig. 5.1) and store the result into the binary image M_d :

Erosion – the image M is scanned for enabled pixels ($m(i, j) = 1$), which are surrounded in all directions by enabled pixels, too. Only these “fully surrounded pixels” will be copied into the eroded binary image M_e .

²This is the reason of the procedure’s name.

Dilatation – each enabled pixel in the image M_e is copied in all of the 8 directions into the resulting dilatated binary image M_d .

5. In the binary image M_d , use a flood-fill algorithm to label all 4-neighbor connected zones by a unique integer label. At the end of this flood-fill, pixels of the same label represent the same blob β .
6. For each β , compute the average of its coordinates $[i_\beta, j_\beta]$ as follows:

$$i_\beta := \frac{\sum_{(i,j) \in \beta} i}{\sum_{(i,j) \in \beta} 1} \quad \text{and} \quad j_\beta := \frac{\sum_{(i,j) \in \beta} j}{\sum_{(i,j) \in \beta} 1} .$$

5.2 Star centroid computation

This algorithm is designed to compute the star centroids more precisely than in the KS algorithm. It is simply the centroid (see Eq. (4.1)) of the pixels forming the star. The only problem in this step is to determine precisely the pixels forming the star, or in other words, the area of the star.

Theoretically, the PSF of a telescope distributes light from a star over an unbounded domain. In practice however, the valuable signal ends up in the noisy background not far from the star center (see Fig. 3.1 on page 13). Therefore, the area of a star is defined as a circle with the center in the star peak and the diameter equal to the *Full Width at Half Maximum* (FWHM). FWHM of a star is defined to be the difference between the two values x_1, x_2 of the star s , at which $s(x_1) = s(x_2) = \frac{1}{2}s_{max}$, where s_{max} denotes the maximum value of s (see Fig. 5.2).

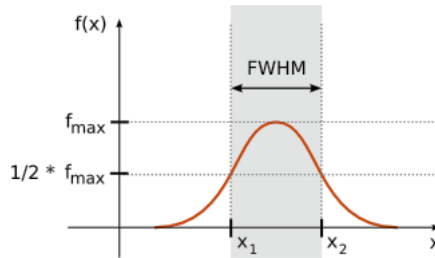


Figure 5.2: Full Width at Half Maximum, [32]

Note that FWHM is a directional-dependent characteristic – there might be different FWHM’s computed from the row-profile of and from the column-profile of a star. However, on well-fabricated optical systems, FWHM is almost equal in all directions, and the average FWHM value is presented as a parameter of the telescope. For the telescope, which acquired the processed data (see appendix B), the value was $\text{FWHM} = 3$ pixels.

The center of the FWHM-circle should be ideally the star centroid, which will unfortunately be known firstly at the end of this algorithm. Therefore, only the estimation $[i_\beta, j_\beta]$ computed in the KS-algorithm 5.1 is taken to be temporarily the center of the FWHM-area.

Before computing the exact centroid of the FWHM-area, its values must be lessened by the average background, i.e. the additive noise n_β . The average background is computed from the ring $R([i_\beta, j_\beta], 2\theta, 3\theta)$, where θ is the half amount of the given FWHM. If the subtraction would produce a value less than zero, zero is considered to be the difference.

The algorithm can finally be described as follows:

1. $n_\beta :=$ average of ring $R([i_\beta, j_\beta], 2\theta, 3\theta)$
2. $A_\beta :=$ Circle $([i_\beta, j_\beta], \theta)$
3. compute the precise centroid $[\bar{i}_\beta, \bar{j}_\beta]$ of A_β :

$$\bar{i}_\beta := \frac{\sum_{(i,j) \in A} i \cdot \max(g(i, j) - n_\beta, 0)}{\sum_{(i,j) \in A} \max(g(i, j) - n_\beta, 0)}$$

similar for \bar{j}_β .

5.3 Star flux computation

Star flux is the total sum of all intensity values lying in the area of the star. Again the area is considered to be a circle of radius FWHM/2, the center, however, is now the precise centroid $[\bar{i}_\beta, \bar{j}_\beta]$ computed in the previous algorithm 5.2.

The algorithm works as follows:

1. $n'_\beta :=$ average of ring $R([\bar{i}_\beta, \bar{j}_\beta], 2\theta, 3\theta)$
2. $A'_\beta :=$ Circle $([\bar{i}_\beta, \bar{j}_\beta], \theta)$
3. compute the total flux β_{flux} of A'_β :

$$\beta_{flux} := \sum_{(i,j) \in A'_\beta} \max(g(i, j) - n'_\beta, 0)$$

where $\theta = \text{FWHM}/2$.

5.4 Strehl ratio computation

As mentioned before, the computation of the Strehl ratio of an image is based on the comparison of the sensed profile of a star (concretely of the star with the largest flux) with the ideal profile, acquirable by the given telescope. There exists a method \mathfrak{M} , based on the article [18], how to compute this ideal profile, i.e. the pure PSF of the optical system. The exact description of this method is outside the scope of this work, however, it might be stated, that the input of this algorithm is a set of the telescope's characteristics: the radius of the primary and secondary mirror, the pixelscale (i.e. how many arcseconds of the celestial sphere represents one pixel) and the characteristic of the used light-filter (i.e. its central wavelength and width). The output of this algorithm is a function called the *Optical Transfer Function* (OTF), what is nothing else then the Fourier image of the system's PSF. Therefore, an inverse Fourier transformation is applied to the OTF, to obtain the final PSF of the telescope.

Having introduced the algorithms 5.1 ("KS"), 5.2 ("Cen"), 5.3 ("Fl") and \mathfrak{M} , the final work-flow of the Strehl ratio computation algorithm can be described as follows:

- Input: image g , a threshold parameter κ , and a set of telescope characteristics (see above).
1. $B = \{\beta\} := \text{KS}(g, \kappa)$; //detect blobs on image
 2. for each $\beta \in B$: $[\bar{i}_\beta, \bar{j}_\beta] := \text{Cen}(\beta)$; //compute centroids
 3. for each $\beta \in B$: $\beta_{flux} := \text{Fl}(\beta, [\bar{i}_\beta, \bar{j}_\beta])$; //compute fluxes
 4. $\hat{\beta} := \text{argmax}_\beta(\beta_{flux})$; //retrieve β with largest flux
 5. $\hat{\beta}_{max} := \text{max}(\hat{\beta})$; //find maximum brightness value of $\hat{\beta}$
 6. Generate the telescope's PSF, using the algorithm \mathfrak{M} and the input characteristics of the telescope.
 7. $p_{max} := \text{max}(\text{PSF})$
 8. $p_{flux} := \sum_{\forall(i,j)} \text{PSF}(i, j)$
 9. Normalize maximums by flux and compute their ratio:

$$q_g := \frac{\hat{\beta}_{max}}{\hat{\beta}_{flux}} \Big/ \frac{p_{max}}{p_{flux}}$$

- Output: the strehl ratio $q_g \in (0, 1)$ of the image g .

The code in the C programming language was overtaken from the ECLIPSE library, [19], deeply revised, and adopted for use on the target telescope.

Chapter 6

Image registration

As to “image registration” it is referred to a process of assembling two or more input images of the same scene into one output image. In general, the images might be taken at different times and/or by different sensors (visible light, infrared, X-ray, etc.). The task in the image registration process is then to find the proper space matching (i.e. to find mutual shift, rotation, scale, skew, etc.) of these images and to combine the pieces of information stored in them into a single output image.

As it has been mentioned in chapter 2, one of the two goals in this thesis is to find and use a suitable registration method for previously chosen well-focused astronomical images.

A broad survey on image registration techniques, done by J. Flusser and B. Zitová in 2003 ([20]), defines two main categories, into which all registration techniques might be classified:

1. Feature-based methods
2. Area-based methods

Methods of the first category are, as the name implies, based on “features”, that might be detected in the input image, like various edges, corners, significant regions, etc. Features detected in the input images are matched on correspondence, whereupon the geometrical transformation of the input images is designed. The images are then transformed and re-sampled, and finally combined in some manner (e.g. by averaging, summarizing, etc.).

In contrast, methods from the latter category do not search for any salient features in the input images. Rather, the content of the window of a preferred size or even the whole image is used for the geometrical transformation estimation. Inside this category, some four sub-categories can be defined, namely: Cross-correlation methods, Fourier methods, Mutual information methods and Optimization methods.

All mentioned image registration methods of both categories search in the first step for mutual geometrical alignment of input images, while in the second step they perform pixel averaging (or similar value-combination). In the case of astronomical images of stars, the first step might be omitted, as the mutual position of the individual input images is known – for each image, its localization on the celestial sphere (the so-called *WCS*, see section 6.1) is pre-computed at image acquisition time. Therefore, registration of images of stars consist only of transforming (re-sampling) them and averaging them – this processing is done by the adopted software package “Montage” (see section 6.2), used for registration of images of stars.

For registration of planetary images, two approaches have been used: again the Montage method, as in the case of stars, and the Cross-correlation method (see section 6.3).

6.1 World Coordinate System

The *World Coordinate System* (WCS) is a way to define the position of an astronomical image on the celestial sphere. What is more, it is a way to map each single pixel of the image to a point on this sphere. Basically, it is a set of keyword-value pairs statements, carried as a sort of meta-data together with the image data in each file. The original paper [21] defines WCS-keywords for expressing various projections and general picture transformations (affine transformation, skew, etc.). In this section, only keywords used by the software of this work are described.

A location of an object on the celestial sphere, known as “astrometry”, is mostly given in the so-called *Equatorial coordinate system*, which is a projection of the Earth’s latitude and longitude onto this sphere. It is expressed as a couple $[\delta, \alpha]$ called *declination* and *right ascension* (or shortly *rectascension*), given originally in arc degrees and hours, respectively, although in many implementations α is expressed in degrees, too. The zero point of this system is taken to be at the vernal equinox, a point derived from the yearly sun path on the sky¹. Declination increases in the northward, right ascension in the eastward direction.

These two coordinates δ and α are stored in the picture-file under the keywords CRVAL1 and CRVAL2, expressing which area of the sky has been photographed. To be concrete, only one single pixel (called the “reference pixel”) of the image is of this precise location – mostly the center of it, although in some cases it can be a different pixel on the image (for example when viewing a certain sub-area of the image). The coordinates of the refer-

¹Though this point slowly moves through the centuries, due to Earth’s precession. Therefore an “epoch”, i.e. a time reference has to be attached. See [22] for a deeper explanation.

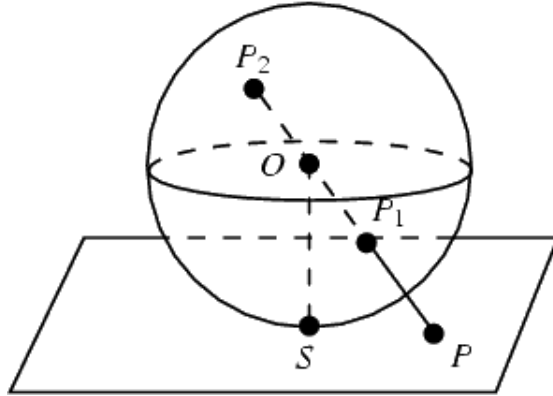


Figure 6.1: Gnomonic projection: the points P_1 (and P_2) are mapped from the sphere surface through the sphere's center O to the point P onto a plane tangential to the sphere (touching the sphere at point S), [28].

ence pixel in the image pixel array are stored under the CRPIX1 and CRPIX2 keywords.

They are two possibilities, how to compute the equatorial coordinates [$\delta = \text{CRVAL1}, \alpha = \text{CRVAL2}$] of the reference pixel (CRPIX1, CRPIX2). The first possibility is to detect at least three so-called reference stars on the picture, i.e. stars with well-known equatorial coordinates, and derive the CRVAL1, CRVAL2 values by some simple triangulation of those coordinates.

The second possibility, how to compute the WCS of the acquired image, is used when no reference stars are present on the acquired image. In such case, the aim of the telescope (given in declination and rectascension) at image acquisition time is taken and the position of the star of interest in the pixel array is added. This method is however much more inaccurate than the first one.

For deducing how the equatorial coordinates [δ, α] of all other pixels are obtained, it firstly has to be stated, that the projection of the celestial sphere to the imaging plane, done by the optical instrument, is not linear. More likely, it is a tangential (gnomonic, rectilinear) projection, as defined in [28], which maps points of sphere surface to a tangential plane (see Fig. 6.1).

If now a matrix of partial derivations of each world coordinate axis (δ and α) with respect to each pixel coordinate axis (i and j), called the *Jacobian*, is computed, then the equatorial and pixel coordinates for each pixel are in following relationship:

$$\begin{pmatrix} \Delta\delta \\ \Delta\alpha \end{pmatrix} = \begin{pmatrix} \frac{\partial\delta}{\partial x} & \frac{\partial\alpha}{\partial x} \\ \frac{\partial\delta}{\partial y} & \frac{\partial\alpha}{\partial y} \end{pmatrix} \begin{pmatrix} \Delta x \\ \Delta y \end{pmatrix}$$

where $(\Delta x, \Delta y)$ is the displacement in pixels from the reference pixel

(CRPIX1, CRPIX2), and $(\Delta\delta, \Delta\alpha)$ is the displacement in arc degrees from the world coordinate (CRVAL1, CRVAL2).

The Jacobian matrix is stored in the image file under the keywords CD1_1, CD1_2, CD2_1 and CD2_2. Although some older images contain instead the keywords CROTA to express the rotation of the image towards the north, and the keywords CDELTA1 and CDELTA2 to express the world coordinate increment at the reference point, the WCS definition document [21] recommends using only CDi_j keywords in all new implementations.

6.2 Registration of images of stars

Having described the World Coordinate System used to localize images of stars on the celestial sphere, the algorithm of their registration can now be introduced. As it has been mentioned before, images of stars are registered by the adopted Montage software system [23], which is designed and optimized for assembling astronomical data into mosaics. Montage produces the resulting image in three following steps:

1. Image re-projection – all images are re-projected to the position of the further final image
2. Common background estimation – differences in background value of the individual input images are levelled (equalized)
3. Image composition – final image is assembled from the re-projected, background-corrected input images

6.2.1 Image re-projection

In the very first step, each input image g_i is re-projected to an image g_r , so that all re-projected images are of the same spatial scale, rotation and gnomonic projection (i.e. are projected on the same tangential plane, see figure 6.2). In other words, the re-projected image is meant to be as close as possible to a picture, which would have been created, if the sky had been observed using an instrument with the final image's pixel pattern.

As it has been stated in section 6.1, a gnomonic projection is a projection of a sphere's surface to a tangential plane, through the sphere's center. In figure 6.2 a single line connects the sphere's center, the original pixel i and its projection $t(i)$ onto the plane T . As stated in [23], this geometric relationship of both tangential planes might be described by transformation equations between the two planar coordinate systems, which require no trigonometry or extended polynomial terms.

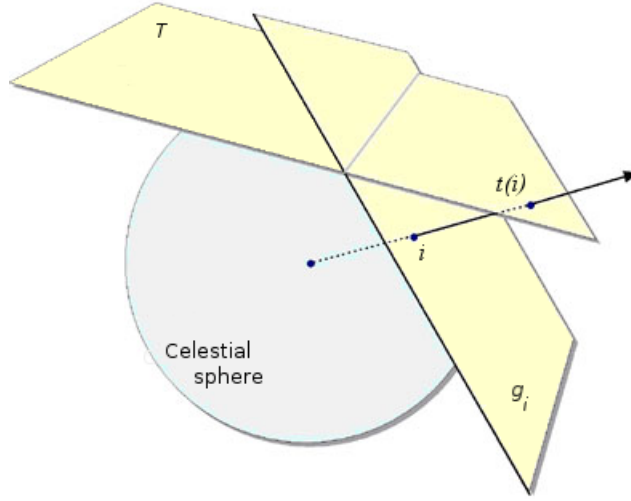


Figure 6.2: Image re-projection. Each input image g_i is re-projected to the same tangential plane T , [33].

After each pixel i of the input image g_i has been re-projected to the pixel $t(i)$, the values of the pixels r of the resulting re-projected image g_r have to be determined (as the projections $t(i)$ mostly do not fit into the pixel grid of g_r). In this determination, it is very important to preserve the total energy flux of the stars as well as their astrometric positions ($[\delta, \alpha]$), if a meaningful astronomical image is desired. Traditional re-sampling methods, such as nearest neighbor and similar are therefore highly inadequate. Instead, Montage redistributes the input pixel energy to the resulting pixel r based on the exact overlap of these both pixels (see Fig. 6.3). The total energy of the resulting pixel is a sum of energies of all input pixels weighted by this overlapping area, formally:

$$v_r = \sum_{r \cap t(i) \neq \emptyset} v_i \cdot s_{r \cap t(i)} \quad (6.1)$$

where:

- i , resp. r denotes the input, resp. resulting pixel
- v_i , resp. v_r denotes the brightness value of pixel i , resp. r
- $t(i)$ denotes the re-projected input pixel
- $s_{r \cap t(i)} \in [0, 1]$ denotes the size of the overlapping area

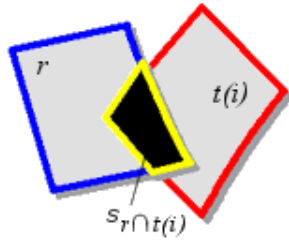


Figure 6.3: The energy of the output pixel r of the re-projected image g_r is proportional to the size of the overlapping area $s_{r \cap t(i)}$ of this pixel and the projection $t(i)$ of the original pixel i , [33].

6.2.2 Common background estimation

Before the re-projected images g_r are assembled into a final output image, they must be corrected for having the same background level. Montage assumes, that the background differences between the individual images can be described by a first-order surface (i.e. a slope + offset) – more complicated background changes cannot be handled with the described background-matching algorithm.

In principle, the correction algorithm is simple: for each image g_r , firstly the set of overlapping areas with the image and its neighbors is determined. Afterwards, each overlapping area is transformed into a difference frame (the brightness values of the neighboring image is subtracted from the values of the processed image). These difference frames are then used in a least-square fit estimation to derive the background correction, which is then used in a half amount to correct the actual background of the processed image (since the neighbors will be processed and corrected, too).

In the present implementation, this process is iterated over all images, until differences for all images becomes appropriately small. The result is a set of images with a common background, ready for assembling.

6.2.3 Image composition

Re-projected and background-corrected images can now be assembled into the final registered image g_f . As it has been mentioned before, it is important to derive the correct energy for each of the final pixels, so that the total star-flux as well as astrometric positions for the imaged stars are preserved.

Therefore, in the process 6.2.1 of image re-projection, when the energy contribution of input pixels are weighted by the area of overlap (see Eq. 6.1), also a cumulative sum S_r of these areas is stored, for each of the resulting pixels:

$$S_r = \sum_{r \cap t(i) \neq \emptyset} s_{r \cap t(i)}$$

The total energy of the pixels f of the final image g_f is then normalized by this cumulative sum:

$$v_f = \frac{\sum_{c \sim f} v_c}{S_r} = \frac{\sum_{r \sim f} v_r}{\sum_{r \cap t(i) \neq \emptyset} s_{r \cap t(i)}} \quad (6.2)$$

where

- v_c is the value v_r from Eq. (6.1) corrected by the background-matching algorithm 6.2.2
- $c \sim f$ denotes that the background corrected pixel c corresponds to the pixel f (i.e. has the same location in the pixel array) of the final image.

6.3 Registration of planetary images

For the registration of images of planets, two different approaches have been used and compared (see chapter 7 for test results): the Montage method, as described in section 6.2, and the Cross-correlation method (CC), which will be described here.

6.3.1 Correlation

The CC registration method is based upon computing statistical correlation between chosen areas on the two images, that should be aligned. Correlation $\varrho(X, Y)$ is a statistical function, measuring the “similarity” of two random variables, X and Y , or more precisely, their linear dependency:

$$\varrho(X, Y) := \frac{\text{cov}(X, Y)}{\sqrt{\text{var}(X)}\sqrt{\text{var}(Y)}} \in [-1; 1], \quad (6.3)$$

where $\text{cov}(X, Y) := E((X - EX)(Y - EY))$ is called “covariance” of the two variables X and Y , and $\text{var}(X) = E(X - EX)^2$ is the “variance” of the variable X . For completeness, EX is the mean value of X , i.e. $EX := \int XP(X)$ where P is the distribution function for X .

Correlation in Eq. (6.3) is defined for random variables. In the case of discrete random variables (i.e. the domain is a discrete set), X and Y are vectors. Images (and their sub-windows) can be considered to be such

vectors. Having two equally-sized image windows W and W' , their covariance is defined as

$$\text{cov}(W, W') := \frac{1}{NM} \sum_{i=1}^N \sum_{j=1}^M (W(i, j) - E(W))^T (W'(i, j) - E(W'))$$

and variance to

$$\text{var}(W) := \frac{1}{NM} \sum_{i=1}^N \sum_{j=1}^M (W(i, j) - E(W))^2.$$

Thus, the correlation of the image windows W and W' can be computed as

$$\varrho(W, W') = \frac{\sum_{i=1}^N \sum_{j=1}^M (W(i, j) - E(W))^T (W'(i, j) - E(W'))}{\sqrt{\sum_{i=1}^N \sum_{j=1}^M (W(i, j) - E(W))^2} \sqrt{\sum_{i=1}^N \sum_{j=1}^M (W'(i, j) - E(W'))^2}},$$

since Eq. 6.3 holds.

As stated in Eq. (6.3), correlation is bounded by -1 and 1 . The value 1 denotes full linear dependency and same orientation of the two vectors. The value -1 also denotes their full linear dependency, but with opposite orientations. Value 0 means that the two vectors are *perpendicular* to each other. Note the similarity with the cosine function of an angle between two Euclidean vectors, which can be computed as

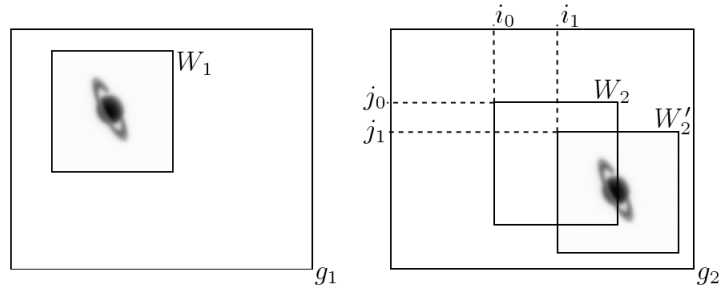
$$\cos(\phi) := \frac{\langle \vec{u}, \vec{v} \rangle}{\|\vec{u}\| \cdot \|\vec{v}\|},$$

where ϕ is the angle between vectors \vec{u} and \vec{v} , and $\langle \vec{u}, \vec{v} \rangle$ is their inner product².

6.3.2 Cross-correlation registration

Having described the correlation of two vectors, the CC-registration method can be introduced. Consider two images, g_1 and g_2 , which are to be registered (see Fig. 6.4). A salient object, or structure is chosen in the image g_1 and clipped to a window W_1 . Now the occurrence of this window in the image g_2 is searched. That is done by aligning the window W_1 on the image g_2 , what defines a sub-area $W_2 \subset g_2$. The correlation of W_1 and W_2 is computed and stored. After all correlations of all possible alignments have been computed

²Indeed, correlation of two random vectors can be considered as a sort of cosine function in the Hilbert space, having the inner product of X and Y defined as $\langle X, Y \rangle := \text{cov}(X, Y)$, what means that the norm is defined to $\|X\| := \sqrt{\text{var}(X)}$.



$$\begin{aligned} \mathcal{C}(i_0, j_0) &= \varrho(W_1, W_2) = 0.2 \\ \mathcal{C}(i_1, j_1) &= \varrho(W_1, W_2') = 0.9 \end{aligned}$$

Figure 6.4: The Cross-correlation algorithm. Window W_2 aligned at $[i_0; j_0]$ has a lower correlation with window W_1 as window W_2' , aligned at $[i_1; j_1]$.

(and form a matrix \mathcal{C} indexed by the individual alignments), the maximum correlation is searched – it indicates the occurrence of W_1 in g_2 and the mutual integer shift of g_1 and g_2 can be derived.

Note that CC is suitable for the registration of mutual shifted images only; no rotation, scale etc. is examined. However, this is not a limitation for the processed data, as during the acquisition time the rotation of the scene is insignificant and no other deformations of the images are present.

To derive a non-integer mutual shift of images g_1 and g_2 , a sub-pixel interpolation of the input images has to be performed. However, this makes sense only if the maximum in the correlation matrix \mathcal{C} is “sharp”, i.e. is significant in value relative to its neighborhood. That was not the case when registering data processed within this work: as shown on Fig. 6.5, no sharp maxima were present in the matrix and therefore no sub-pixel accuracy has been performed in the CC-registration algorithm.

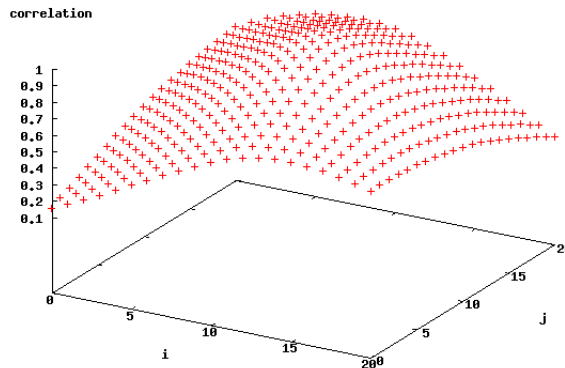


Figure 6.5: The correlation matrix \mathcal{C} . No sharp maxima were detected.

Chapter 7

Experiments and tests

In order to attain the thesis goals (see section 2 on page 11), i.e. to choose a suitable focus measure and registration technique and in order to measure the performance of the choice, several tests have been done. It has to be proven, that on the processed data the introduced focus-measures perform well, and that the registration technique improves the angular resolution of the given telescope.

Unfortunately, during the works on this thesis many technical problems arose on the observatory in Granada, Spain and its telescope IR (see appendix B) delivering data for this work¹. Due to these problems, very little real data could have been obtained and processed by the produced LI-software. This lack of data results therefore in a poor exploration of the software performance and its abilities.

However, some tests have been done, and as will be shown in this chapter, they are more or less promising (although no angular resolution enhancement has been achieved). Nevertheless, much more testing must be done in the future (see chapter 8 for future works proposals) to tune-out the software and use it for the desired goal – angular resolution enhancement comparable to adaptive optics or space-based telescopes.

7.1 Experimental part

In this part, the results of controlled experiments are presented. Artificially and naturally defocused data are measured by the focus-measures described in chapters 4 and 5 in order to demonstrate their performance and limitations. In the case of planetary focus measures M_1 (gray level variance), M_4 (moments-measure) and M_5 (wavelet measure), a “best” one has to be chosen

¹One dataset has been therefore acquired by the WATCHER telescope, placed in the Republic of South Africa, see appendix B.

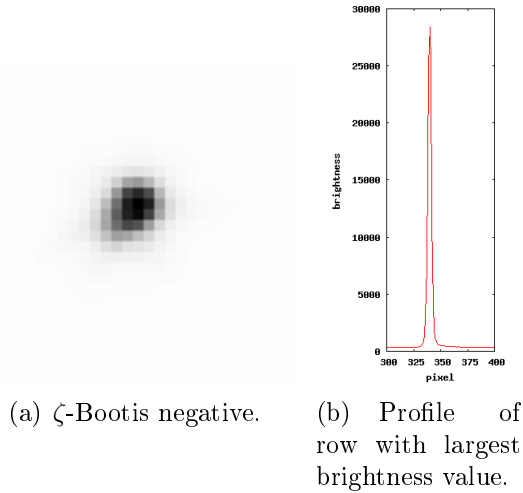


Figure 7.1: Negative of ζ -Bootis and its row-profile. Original brightness values of the star range from 0 to 28386.

to be used in the LI-software. The criterion will be the discriminability, i.e. variation of values with respect to blurring.

7.1.1 Artificial blurring

The artificial blurring of data should confirm, that the focus-measures satisfy the requirements stated in chapter 4 (page 15), foremost monotonicity. The focus-measures are not tested on blurred artificial data, as they performance are described in the referenced sources. Rather the applicability on real data is examined, therefore the measures are applied on artificially blurred images of stars and planets. In the first experiment, both types of images are convolved by a growing square mask, in the second experiment by a Gaussian mask.

Images of stars

The experiment has been done on the image of the star ζ -Bootis (Fig. 7.1(a)) in the Bootes-constellation. It is a double-star, i.e. it is composed of two stars rotating around common gravitational barrycentrum (with a period of 123 years, [29]). Both individuals are on the sky less than one arc second apart. As stated in appendix B, the pixelscale of the IR-telescope is 0.69 arcseconds/pixel, what means, that ζ -Bootis takes in the ideal case less than 1.5 pixel on the image. As can be seen on Fig. 7.1(a), the area taken by ζ -Bootis is approximately 4-5 pixels in the south-east direction, which is caused by the atmosphere turbulation and a relative long exposure time of the IR-camera (250 ms, i.e. the frame rate is 4 FPS).

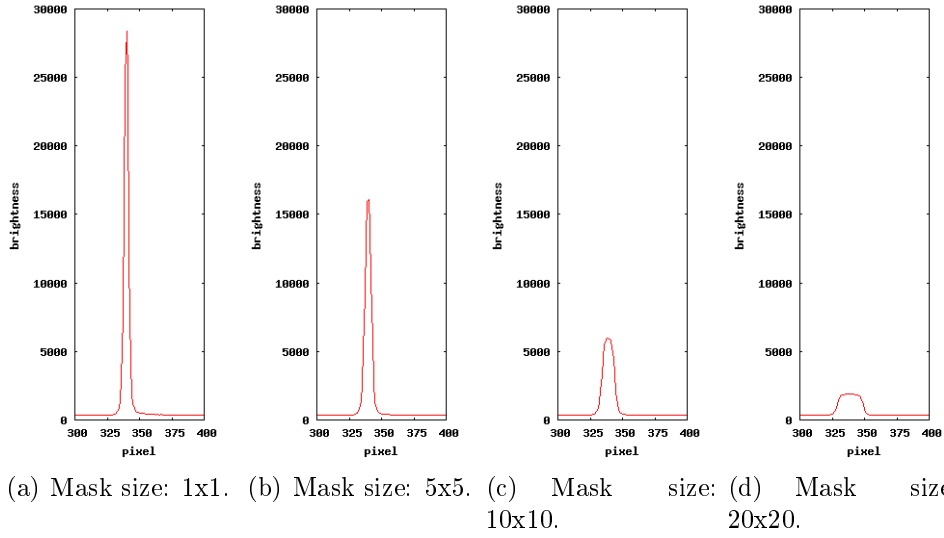


Figure 7.2: Row profiles of ζ -Bootis after convolution with square mask of growing size.

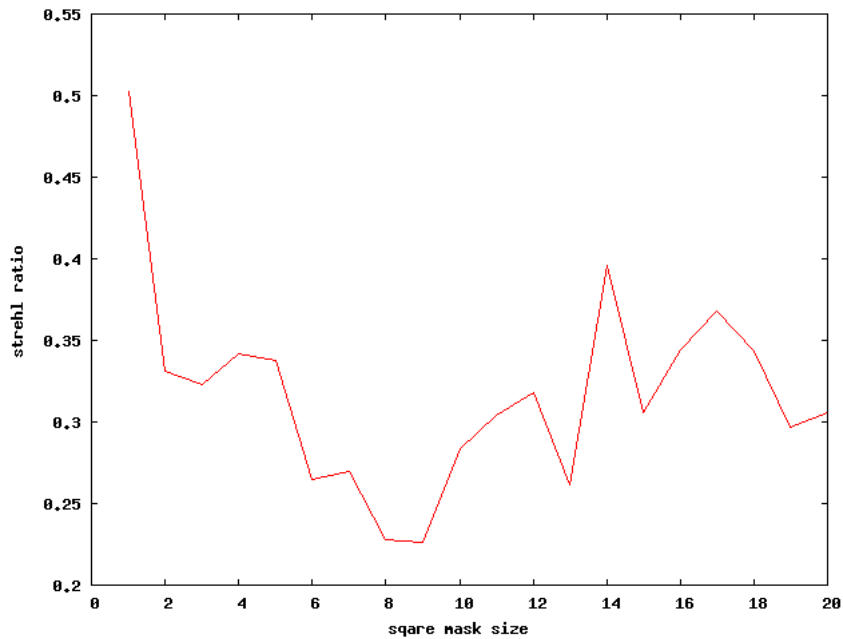


Figure 7.3: The strehl ratio of square-convolved images of ζ -Bootis. Monotonicity is strongly deteriorated after the mask is greater than 9x9.

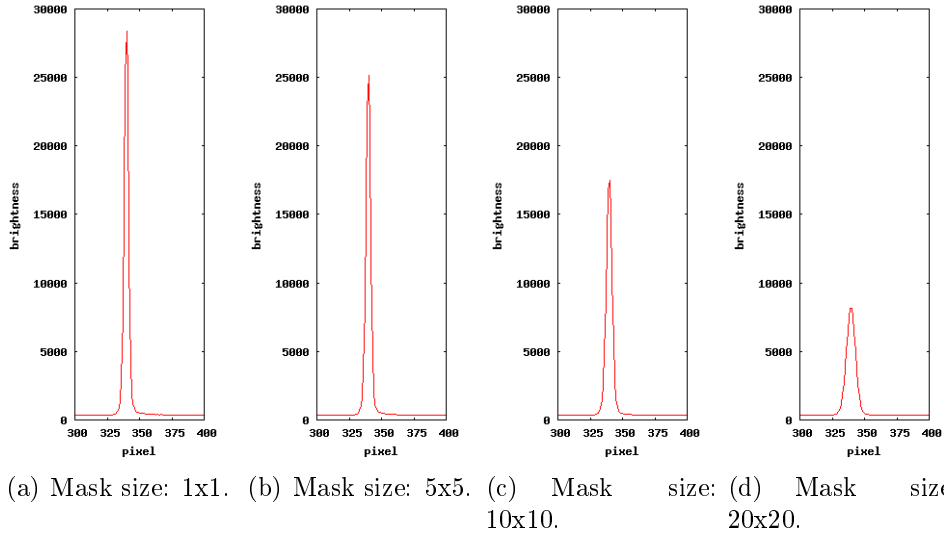


Figure 7.4: Row profiles of ζ -Bootis after convolution with Gaussian mask of growing size.

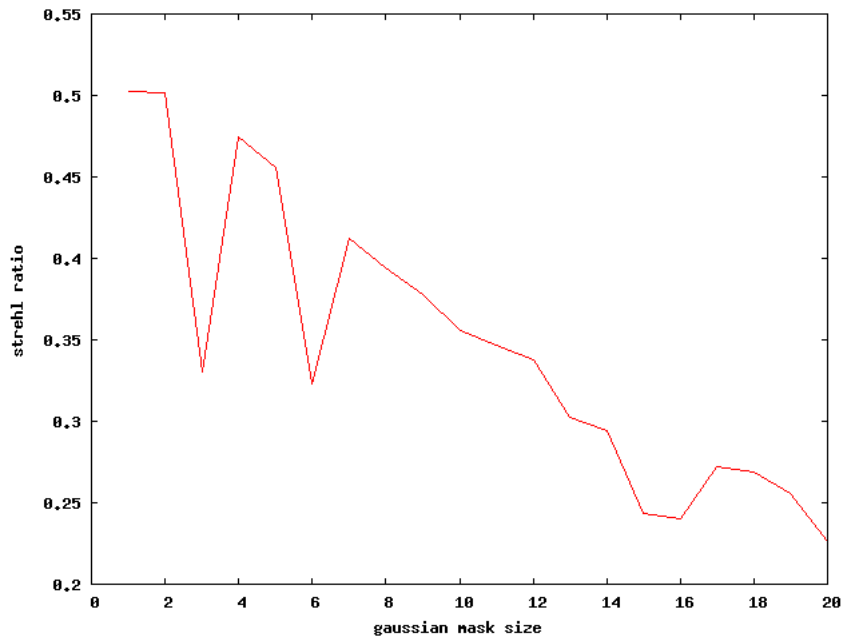


Figure 7.5: The Strehl ratio of Gauss-convolved images of ζ -Bootis. Monotonicity is relatively well retained, although three breaches can be observed (at mask size 3, 6 and 15-16).

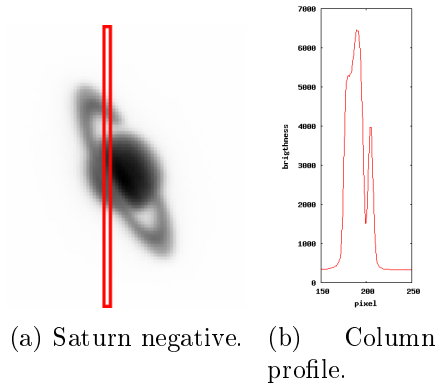


Figure 7.6: (a) A typical picture of Saturn processed in this thesis (a negative). Red marked column is imaged on (b). Original brightness values of the imaged picture range from 0 to 7917.

The convolution with a growing square mask results as expected in a weakened contrast and a larger FWHM of the imaged star (see Fig. 7.2). The Strehl ratio of such convolved stars can be seen on Fig. 7.3. The graph loses its monotonicity for masks larger than 9×9 . Square convolution, however, does not approximate atmospheric turbulences very truly, therefore this bad result is not surprising.

A Gaussian mask convolution does a better approximation of these turbulences. As can be seen on Fig. 7.4, again the contrast of row-profiles are weakened by the growing mask size, but the degradation is slower and the FWHM of the star does not change so significantly as in the case of square mask convolution. The Strehl ratio of such convolved images can be seen on Fig. 7.5, where a much better monotonicity can be observed, although three times distorted.

Images of planets

The only planet available for the experiments and tests in this work is Saturn. In spring 2007, when the datasets were shot, it was $1,4 \cdot 10^9$ km from Earth away, what means that it took approximately 17.5 arcseconds on the sky. With the same pixelscale 0.69 arcseconds per pixel it means, that on the processed pictures, Saturn was 25-26 pixels in diameter (taken without the rings). A typical picture of Saturn processed within this work is shown on Fig. 7.6(a).

Saturn has a significant exoplanetary structure – its rings. Therefore the examined column is not that with the largest value, as it has been in the case of ζ -Bootis, but such a one, which comprises the planet as well as the rings (see Fig. 7.6(b)).

Convolution with square mask again causes heavy damage, which makes

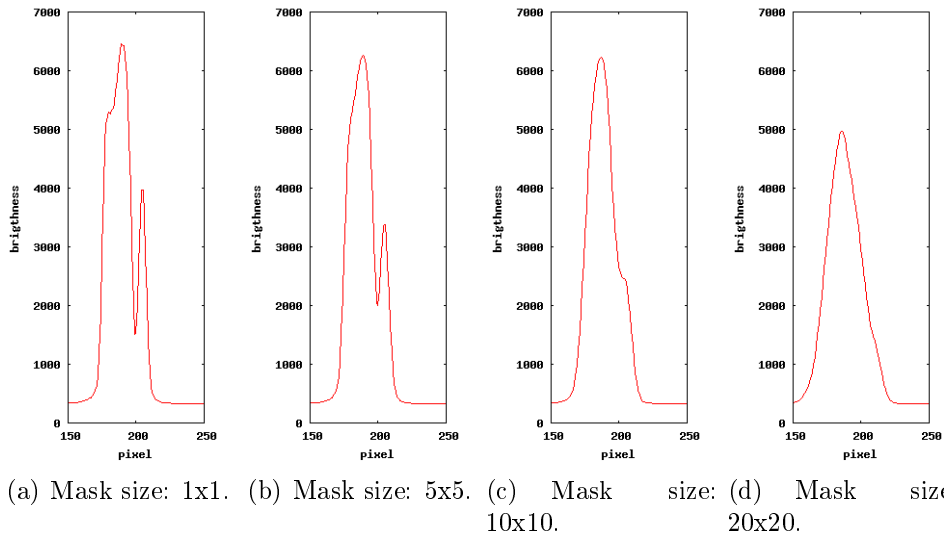


Figure 7.7: Column profiles of Saturn after convolution with square mask of growing size.

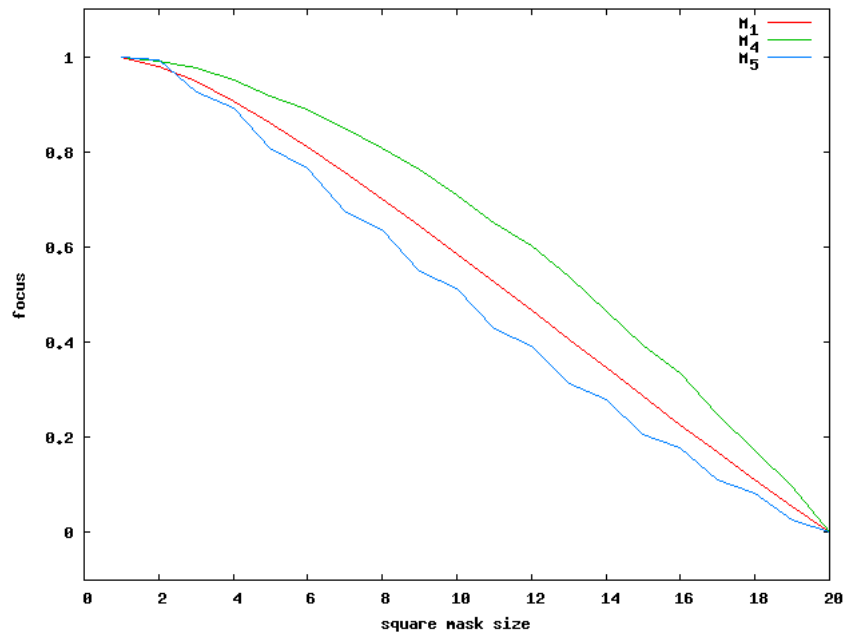


Figure 7.8: The measures M_1 , M_4 and M_5 applied to the square-convolved images of Saturn. Monotonicity of all three measures is undistorted. Note that M_4 is a blur measure and originally grows with growing mask-size – here the values of M_4 have been reverted (maximum value became minimal and vice versa).

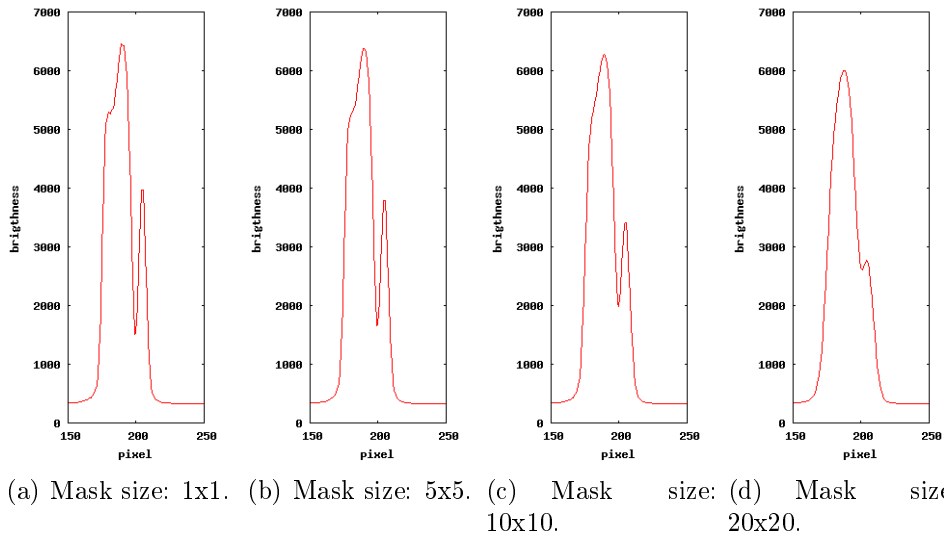


Figure 7.9: Column profiles of Saturn after convolution with Gaussian mask of growing size.

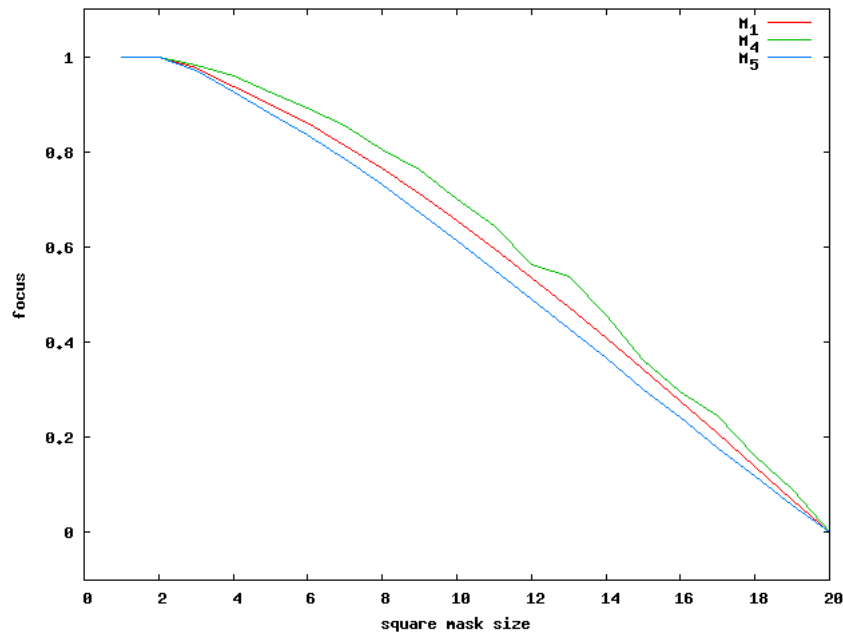


Figure 7.10: The measures M_1 , M_4 and M_5 applied to the gauss-convolved images of Saturn. Monotonicity of all three measures is undistorted. Note that M_4 is a blur measure and originally grows with growing mask-size – here the values of M_4 have been reverted (maximum value became minimal and vice versa).

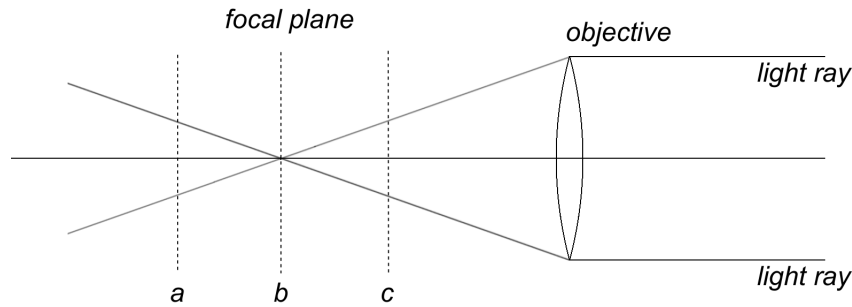


Figure 7.11: Natural defocusation: positions a and c are extreme displacements of imaging plane from the focal plane (position b).

Saturn unrecognizable already by a mask with size 10×10 (Fig. 7.7). Nevertheless, all three focus-measures M_1 , M_4 and M_5 are perfectly monotonical, although M_5 little bit stepwise (Fig. 7.8).

Gaussian masks are again less destructive to the image content as can square masks (see Fig. 7.9). This results in a better, smoother performance of the measure M_5 against square convolution (Fig. 7.10).

In both cases (square and gauss mask convolution) the M_5 measure shows slightly better discriminability as M_1 and M_4 . If this property of M_5 will be preserved in further tests, it is a good candidate to be the focus-measure used in the final LI-software.

7.1.2 Defocusation

The third experiment is similar to the first two (square and gauss mask convolution), except that the focus-measures are being run on naturally defocused data. Natural defocusation is obtained, when the image plane is displaced from the focal plane of the telescope (Fig. 7.11). Datasets processed in following experiments have been obtained by taking several tens of photographs of the observed object with a moving imaging plane. In the beginning the imaging plane is behind the focal plane (position a on Fig. 7.11), then slowly moves towards the focal plane, passes it (position b on Fig. 7.11) and finally ends up in front of the focal plane (position c on Fig. 7.11). The data taken are therefore at the beginning strongly defocused, than grow on focus, approximately in the middle of the way they are perfectly focused, and then again loose focus to finally end up again strongly defocused. The value of the imaging plane position of the given photograph is stored in the keyword FOC_POS in the meta-data file header – this keyword is therefore used also in the future text to reference the imaging plane position.

A good focus measure should be, so-called, *unimodal* on such data, i.e. it should reach one and only one maximum.



Figure 7.12: Object with fourth largest strehl (0.539898) is too defocused (imaging plane position 9809).

Images of stars

The experiment has been done on images of RX-CRUX, which is a single star in the constellation Crux in the southern hemisphere acquired by the WATCHER telescope. FOC_POS ranges from 9609 to 10609 with a step of 20 units. The focal plane of the telescope is at FOC_POS = 10060, therefore the focus measure should reach its maximum as close as possible to this position.

Strong defocussation of point light-sources produces well-known “donuts”, as seen on Fig. 7.13. Such “donuts” do not satisfy requirements on the shape of a star, i.e. they can not be approximated by a Gaussian “hat” (see Eq. (3.1) on page 13 for a more precise definition). Therefore their strehl ratio is unpredictable, as subareas considered to be stars can achieve good ratios of peaks relative to their extent, which is the cause of a good strehl.

Fig. 7.14 shows the evaluation of strehl ratio due to the defocussation. The computed maximum at FOC_POS = 10129 does not perfectly agree with the expected maximum at FOC_POS = 10060. Monotonicity is relatively preserved in the range of FOC_POS \in [9909; 10389]. Outside this range, defocussation is too strong, and the strehl ratio is a false computation. The object causing second spike from the left (imaging-plane position 9809) is shown on Fig. 7.12 – it is a too defocused “donut”.

Images of planets

For the experiment on naturally defocused planets, again only the planet Saturn is available, however in three different datasets. The first dataset “A”, taken on 27.02.2007 is a good sequence of images with FOC_POS ranging from 7440 to 8722 with a step of cca. 10-12 units². As can be seen on Fig. 7.15, defocussation stops growing by positions more than 200 units away from the focal plane. The focal plane of the telescope is at cca. FOC_POS = 8100, therefore maximal values of focus measures are expected at this point.

²The inaccuracy of the step size is of hardware origin.

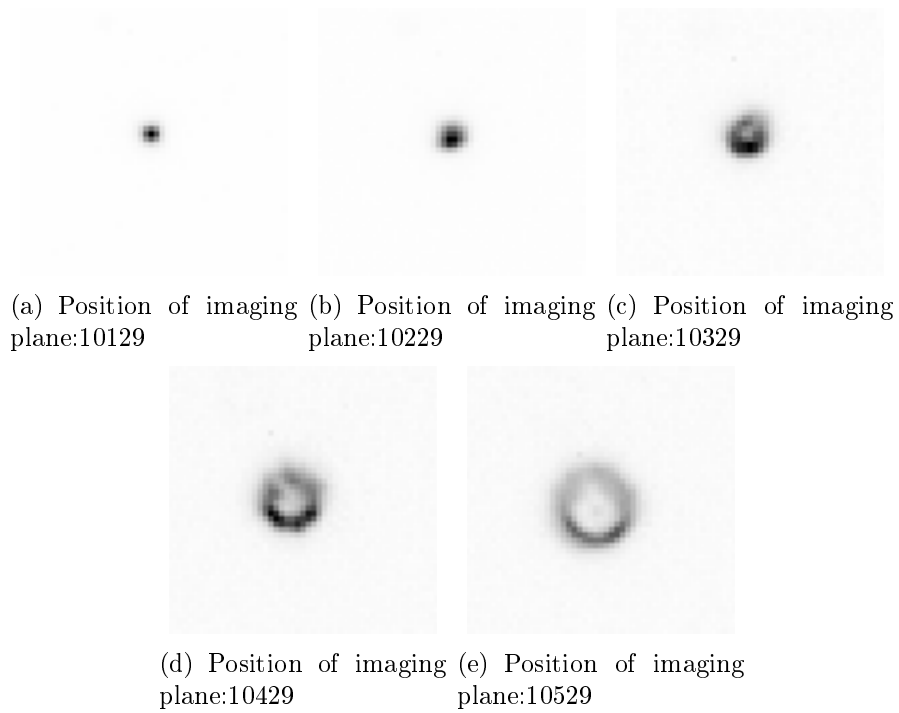


Figure 7.13: Natural defocusation of RX-CRUX. Typical “donuts” can be seen on high defocusation.

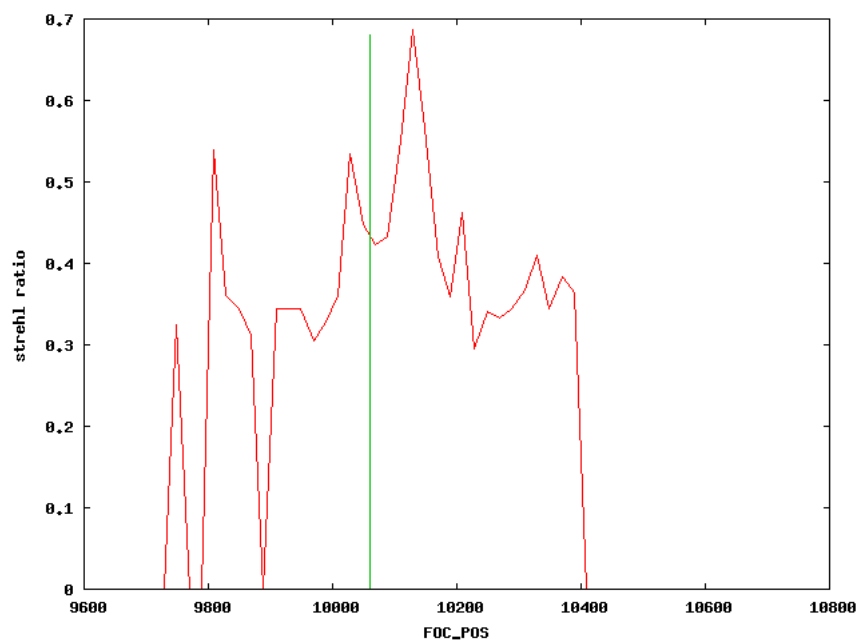


Figure 7.14: The strehl ratio of natural defocused RX-CRUX dataset. The ideal position of the imaging plane is 10060 (vertical line).



(a) Position of imaging plane: 8100 (b) Position of imaging plane: 7900 (c) Position of imaging plane: 7685 (d) Position of imaging plane: 7463

Figure 7.15: Natural defocusation of Saturn (dataset A). The differences among strongly defocused images (c and d) are minimal.

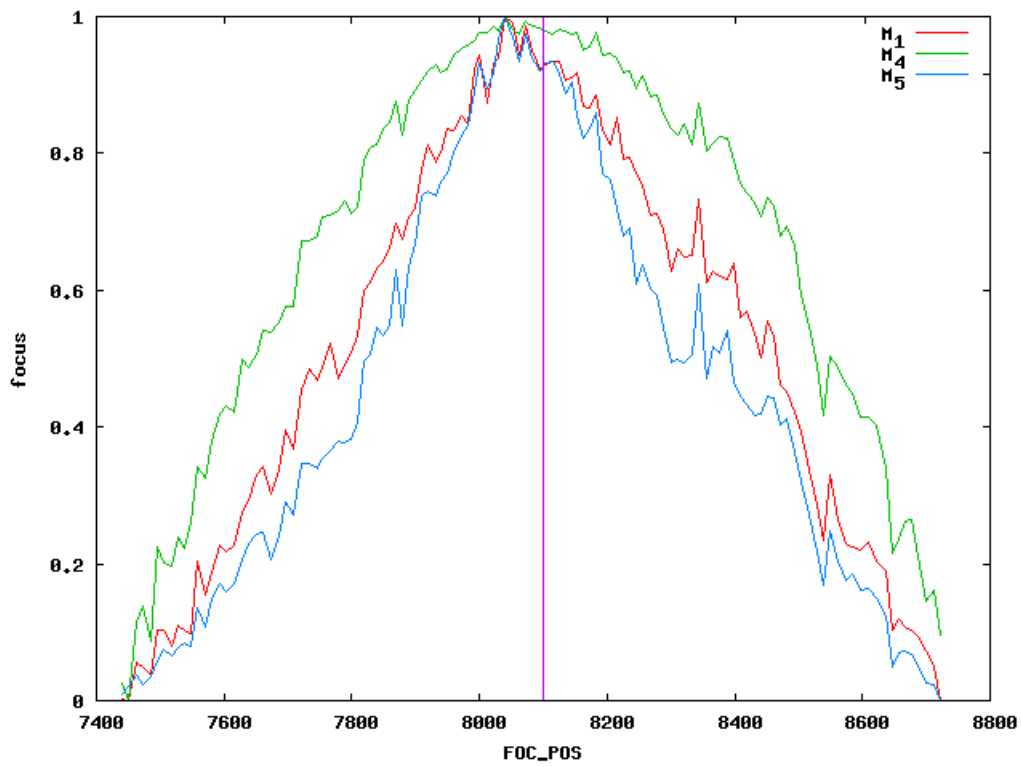


Figure 7.16: The measures M_1 , M_4 and M_5 applied to naturally defocused Saturn images (dataset A). The ideal position of the imaging plane is 8100 (vertical line).

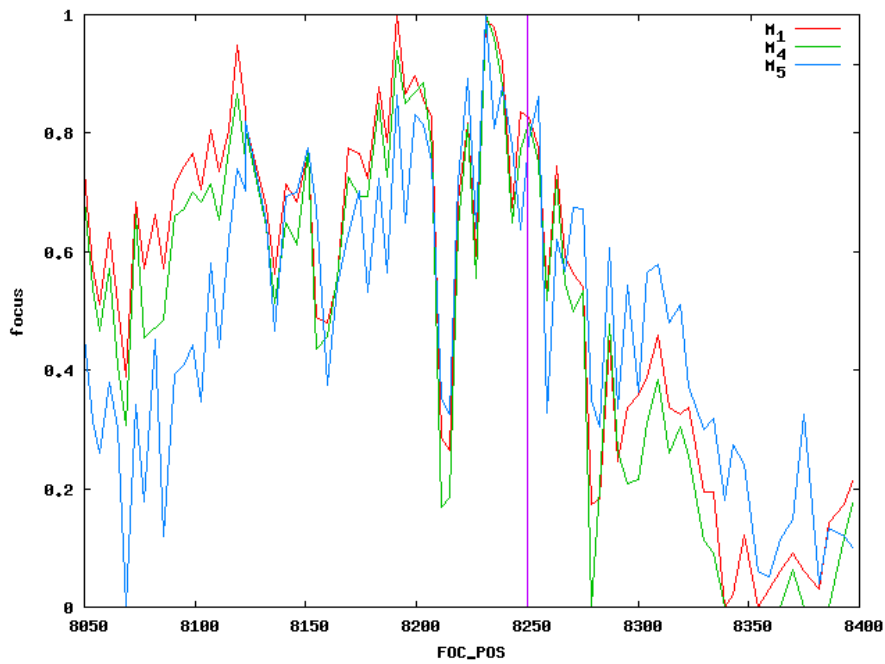


Figure 7.17: The measures M_1 , M_4 and M_5 applied to naturally defocused Saturn images (dataset B). The ideal position of the imaging plane is 8250 (vertical line).

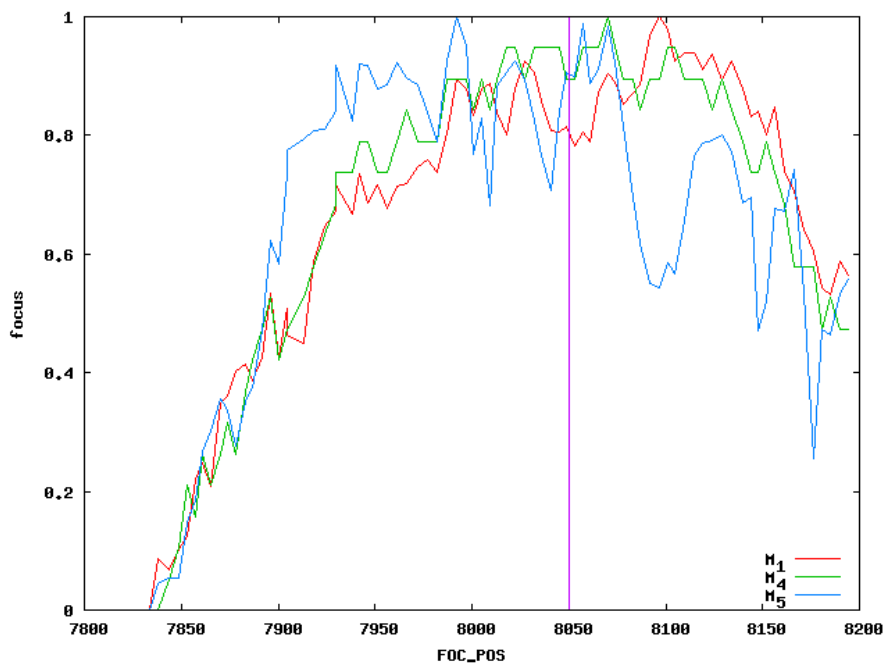


Figure 7.18: The measures M_1 , M_4 and M_5 applied to naturally defocused Saturn images (dataset C). The ideal position of the imaging plane is 8050 (vertical line).

Fig. 7.16 shows the evaluation of M_1 , M_4 and M_5 on the dataset A: monotonicity and unimodality (only one maximum) is well preserved, and all three evaluations are approximately of the same shape. All measures agree in the computed maximum (FOC_POS = 8041), although it does not match the expected maximum (FOC_POS = 8100) exactly. As in the case of mask convolutions, M_5 again shows best value variation.

The second dataset “B” has been taken on 1.5.2007. Saturn is rendered much more weaker than in other datasets and the images contain also more noise, due to a different camera configuration. FOC_POS ranges from 8050 to 8397 with a step of cca. 4 units, where position 8250 is the position of the focal plane. The evaluation of the three measures M_1 , M_4 and M_5 on this dataset is shown on Fig. 7.17: perhaps due to a greater Signal-to-noise ratio the monotonicity is much more distorted than in the case of dataset A. Also unimodality is breached (two spikes can be observed). However, measures agree more or less in their shapes, what supports the thesis of bad data (and not bad measures). Note that dataset B has a smaller range of FOC_POS than dataset A, what means it shows a more detailed segment of the evaluation (i.e. in a greater “zoom”).

The third dataset “C” is a set of pictures, where each 10 consecutive images have the same FOC_POS value. Each image is evaluated on focus, and then the values of the given type (M_1 , M_4 or M_5) are averaged. It is a attempt to eliminate the instability of the monotonicity due to noise and another defocussation caused by the atmosphere.

Dataset C has a FOC_POS ranging from 7834 to 8194 with a step of cca. 5 units. Expected maximum of focus is at FOC_POS = 8050. The evaluation of M_1 , M_4 and M_5 is shown on Fig. 7.18: monotonicity of M_1 and M_4 are better than monotonicity of M_5 . What is more surprising, measures do not agree on a common maximum and M_5 is not even unimodal (three spikes present on the graph).

7.2 Tests on real data

This section brings the results of testing the produced Lucky-imaging software. One dataset of star-images (2000 images of ζ -Bootis taken at 8.5.2007) and one dataset of planetary images (2000 images of Saturn taken at 8.5.2007) has been acquired. All images have been taken in the focal plane of the telescope, so only blur introduced by the atmosphere is present.

The test have been done as follows: All images have been measured on focus with the respective focus-measures, $n\%$ of the best focused images have been taken and registered into a single output image. The parameter n was gradually set to 1%, 2%, 5% and 10% (100% selection was not processed, as the registration of 2000 images would take approximately 24 hours) to

demonstrate the relevance of the parameter on the quality of the produced output.

7.2.1 Lucky imaging of ζ -Bootis

The 2000 input images have been measured on focus by the strehl-ratio measure. The result can be seen on Fig. 7.19: strehl ratios vary from 0.686816 to 0.235844, observable is one dominant peak, and five to six minor peaks. Fig. 7.20 shows the same strehl ratios, but sorted: the three lines mark the 2%, 5% and 10% limit of the best focused images (the 1% limit is not marked due to little space).

The results of the registration of varying $n\%$ best focused images can be seen on Fig. 7.21: for the human eye, the images show no differences. The parameter n does not seem to have an influence on the image quality. Finally, the individual stars forming the double-star ζ -Bootis cannot be distinguished – the produced images still show just a “blot”, although of elliptical shape (what indicates, that it is not a common single star).

When looking on the row profiles, containing the pixel with the highest brightness value (Fig. 7.22), difference of quality of individual images can be observed. The 1%-selection produces a slightly better profile of the star as the other three selections (2%, 5% and 10%), although a worse profile than the best input image. More precisely, the strehl ratios of the 5 examined images are:

Image	Strehl ratio
best input image	0.6868
1%-selection	0.6011
2%-selection	0.5674
5%-selection	0.5578
10%-selection	0.5557

Table 7.1: Comparison of $n\%$ -selection influence on strehl ratio.

After examining row profiles of produced images, it can be claimed, that the parameter n in fact *does* have an influence on the image quality produced; as expected, growing n causes worse and worse star profiles and strehl-ratios of the assembled images.

Let us reconsider the negative result, that the double star ζ -Bootis has not been resolved into its individuals. As stated in subsection 7.1.1, the individuals are less than one arc second apart. Because the telescope’s pixelscale is only 0.69 arcseconds per pixel and its FWHM is 3 pixels (see appendix B), both individuals are on the image only 1.5 pixel apart, while covering

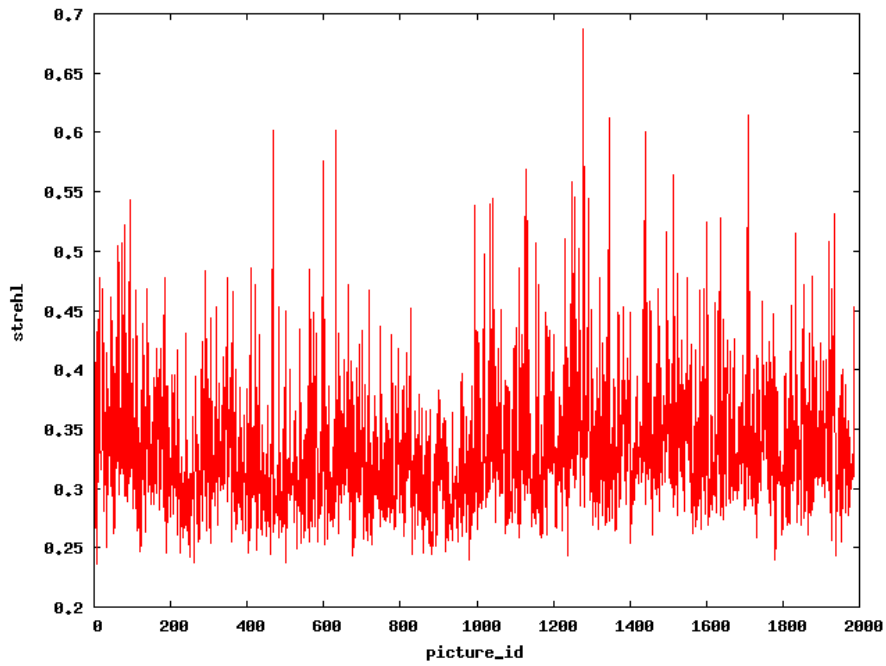


Figure 7.19: Strehl ratio of the ζ -Bootis dataset.

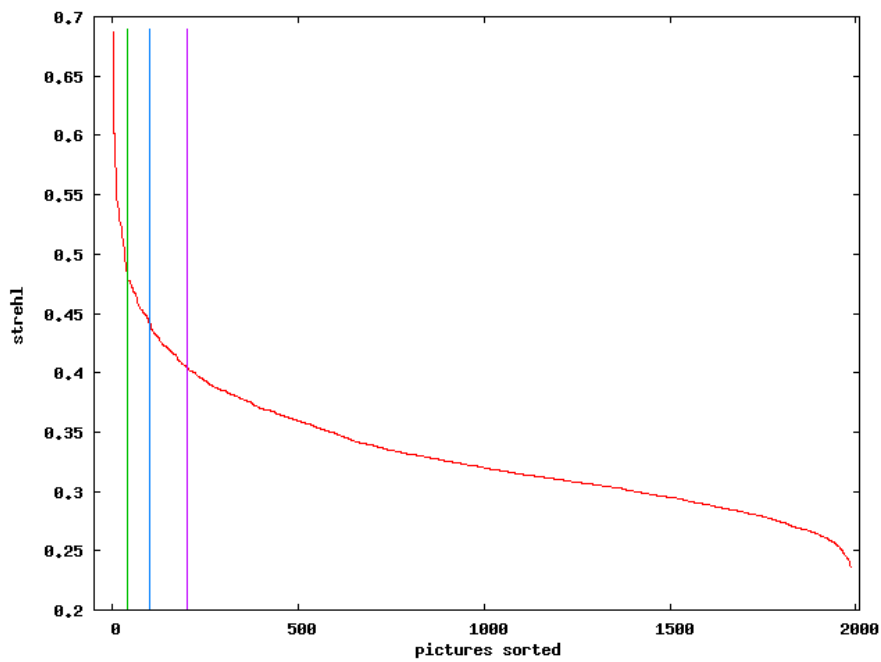


Figure 7.20: Strehl ratio of the ζ -Bootis dataset, sorted by this ratio. The vertical lines mark the 2%, 5% and 10% limit of images with best focus.

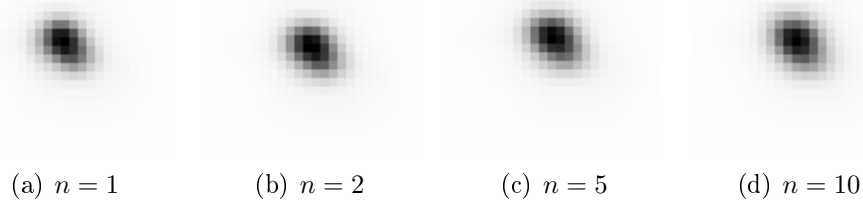


Figure 7.21: Output images of LI-software run on the ζ -Bootis dataset with varying n (negatives). No significant differences can be observed.

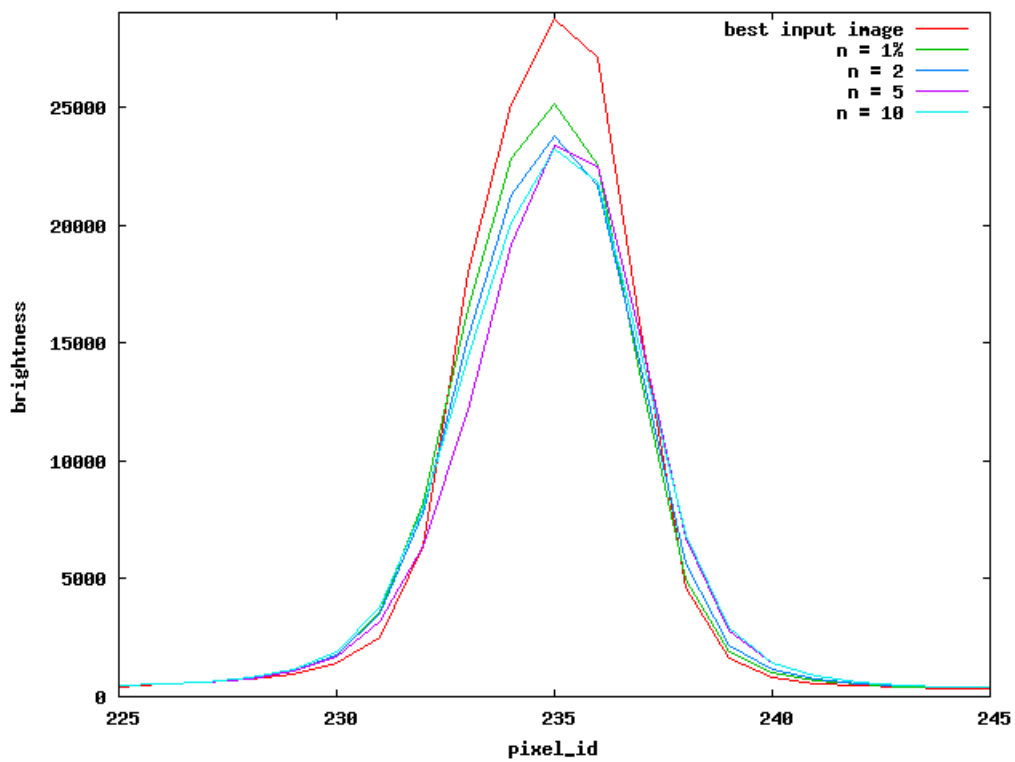


Figure 7.22: The row profiles of the best input image (shown on Fig. 7.1(a), page 36) and the LI-output images (shown on Fig. 7.21).

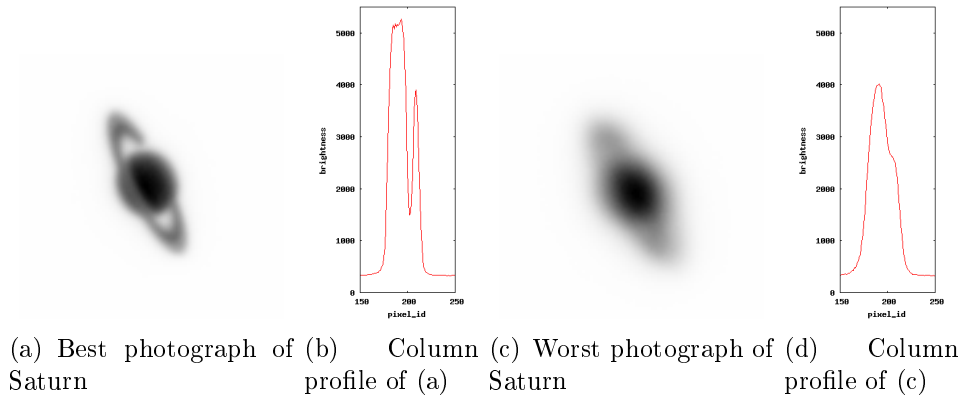


Figure 7.23: Best and worst saturn due to the measure M_5 (negatives).

the area of approximately 3×3 pixels. It is nearly impossible to resolve the double star into its individuals even in the ideal case (i.e. no atmosphere would cause image blur) at this low sampling. The telescope used is simply too weak (its pixelscale is too low) to resolve the given target ζ -Bootis.

7.2.2 Lucky imaging of Saturn

The 2000 images of Saturn have been evaluated on focus by all three measures M_1 , M_4 and M_5 . The result of the evaluation can be seen on Fig 7.24: all three measures agree well in shape, although not exactly in the peak; M_1 considers picture number 826 to have the best focus, M_4 picture number 1685 and M_5 number 1827. Fig. 7.25 shows the same focus evaluation, but sorted. M_5 again shows greatest discriminability (decreases most quickly). The three lines mark the 2%, 5% and 10% limit of the best focused images (the 1% limit is not marked due to little space).

After the evaluation of focus, $n \in \{1, 2, 5, 10\}$ percent of best focused pictures have been registered once with the CC-algorithm and once with the Montage algorithm (both algorithms are described in chapter 6 on page 26) to compare both approaches.

The best and the worst focused photographs due to M_5 are shown on Fig. 7.23. The attached profiles of columns passing the planet and the rings (see Fig. 7.6(b)) confirm the picture quality difference. However, after images have been registered and averaged, no such differences can be observed, even for various n (see Fig. 7.26) – for the unweaponed eye all output images seem to be of the same quality (although a little more blur can be observed on the 10%-selections than on the 1%-selections). On the respective column profiles of all the 8 output images (see Fig. 7.27) only minor differences can be observed, too.

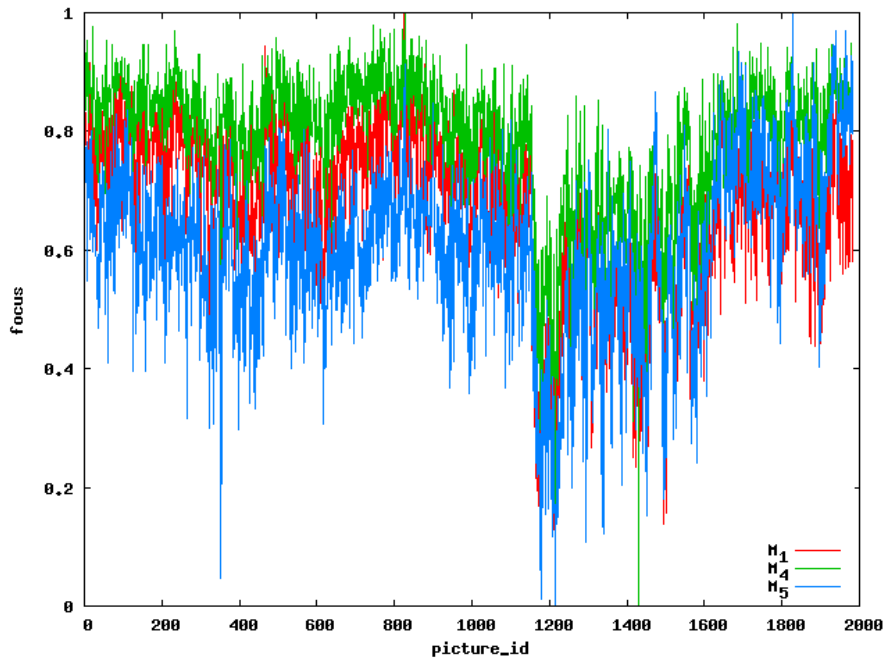


Figure 7.24: The measures M_1 , M_4 and M_5 applied to images of Saturn.

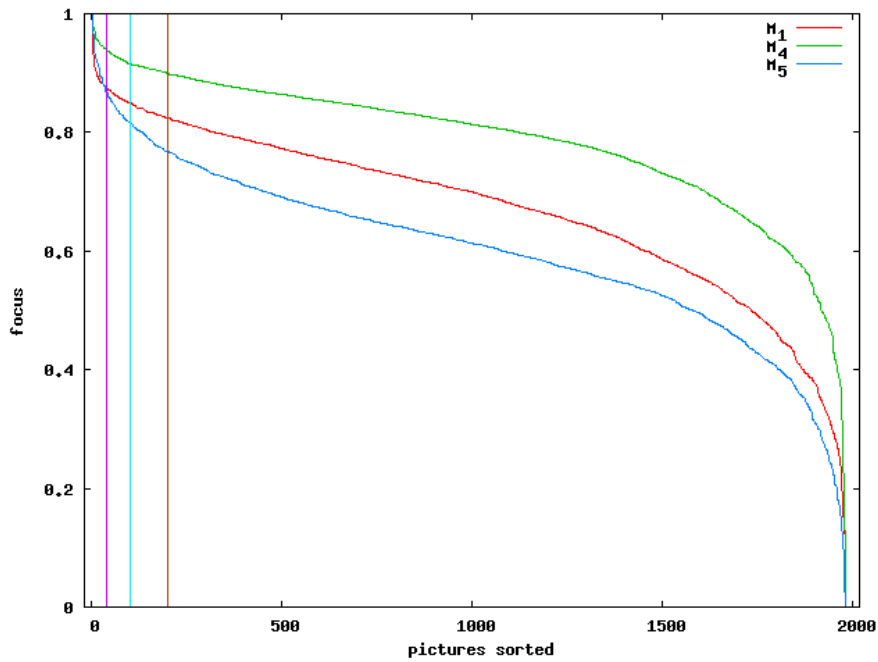


Figure 7.25: The measures M_1 , M_4 and M_5 applied to images of Saturn, sorted by this measures (respectively). The vertical lines mark the 2%, 5% and 10% limit of images with best focus.

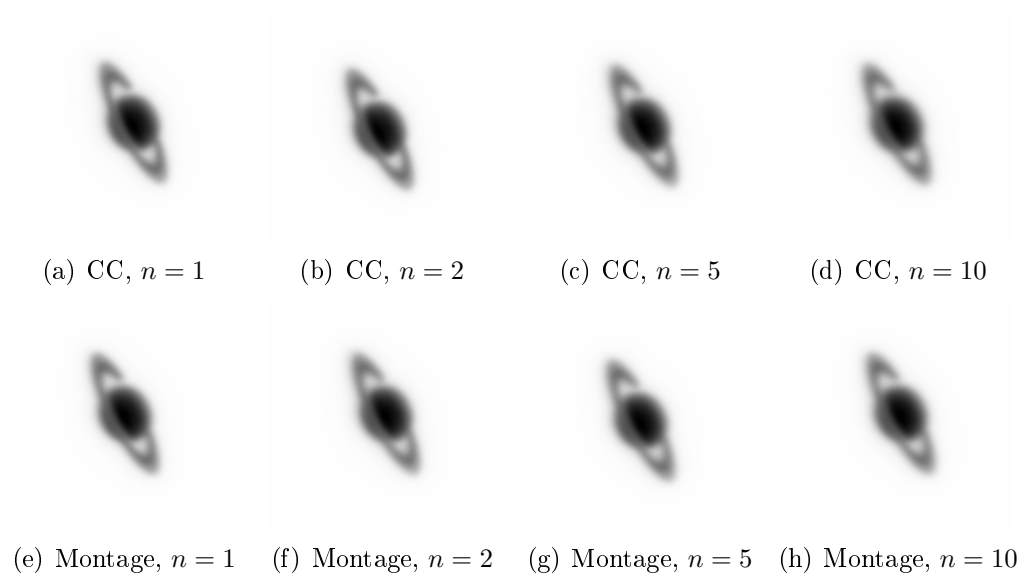


Figure 7.26: (a)-(d): CC registration output with varying n ; (e)-(h): Montage registration output with varying n . Differences are minimal, only observable between $n = 1$ and $n = 10$.

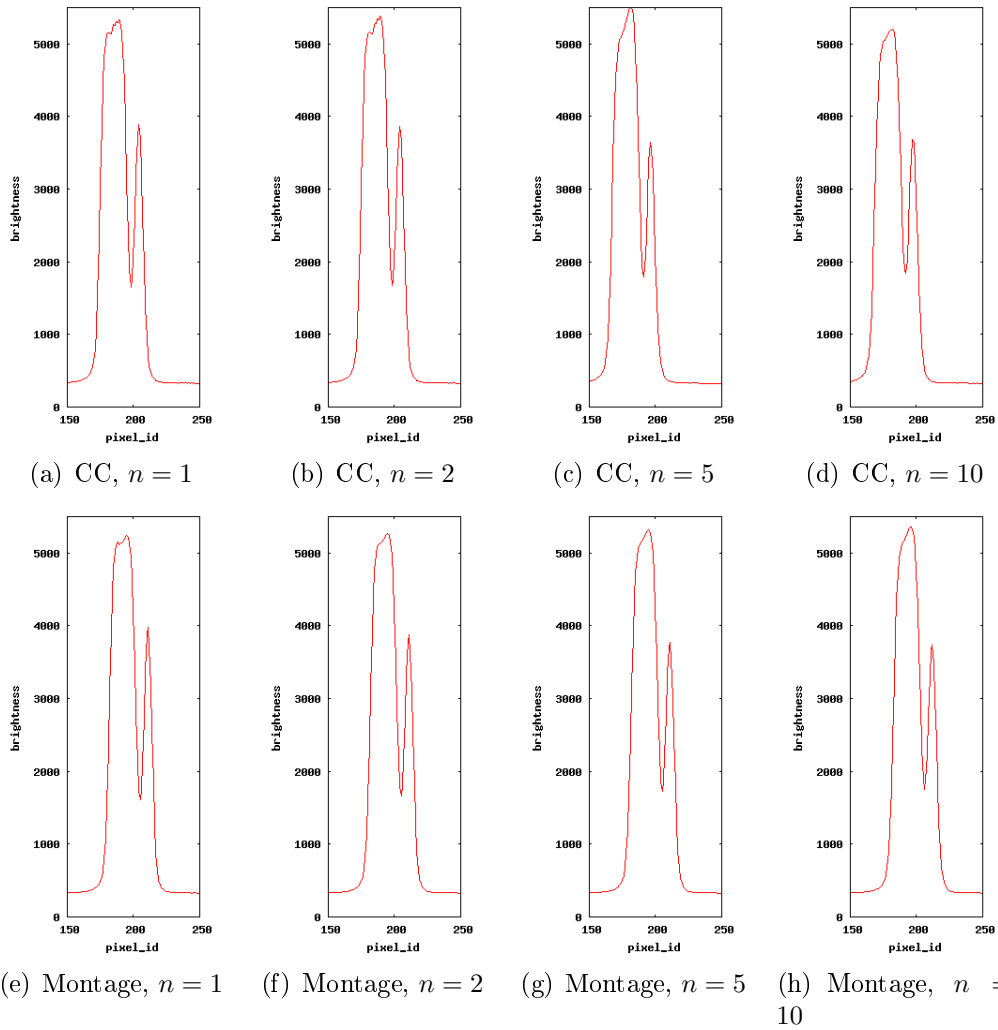


Figure 7.27: (a)-(d): Column profiles of CC registration output with varying n . (e)-(h): Column profiles of Montage registration output with varying n . Differences are minimal, apparent only between $n = 1$ and $n = 10$.

7.3 Conclusion of tests and experiments

In this chapter, four focus measures and two registration techniques have been used to process astronomical images. This section brings the comparison of the performance speed and quality of these algorithms. All computations have been done on a machine with the configuration Intel Celeron 1500 MHz, 512 MB RAM.

Among areal focus-measures, in most cases M_5 performed the best, especially in manner of discriminability. However, as can be seen on table 7.2, M_5 is noticeably slow, in comparison with the other two measure. Except of the wavelet decomposition, also transformation into different file-formats (acquired .fits into processed .mat) consumes time.

measure	number of photographs	computation time
strehl ratio	51	0 min 29 sec
M_1	51	0 min 07 sec
M_4	51	1 min 25 sec
M_5	51	8 min 42 sec

Table 7.2: The comparison of computation speed of strehl ratio, and the focus measures M_1 , M_4 and M_5 .

In the case of M_4 , the file-format also has to be transformed, what is more, the object of interest has to be detected and cropped out (as M_4 performs only on zero-background images, see chapter 4). The computation itself is relatively fast, but with the worst discriminability.

We recommend therefore to use M_1 for measuring focus of planets and other areal objects, as the discriminability is sufficient, and the speed extremely fast.

The two image registration techniques are compared in the table 7.3. Montage shows a great computational complexity, growing with the amount of processed photographs. On the other hand, Montage uses non-integer pixel transformation, therefore has a better accuracy of the assembled images.

N	number of photographs	CC	Montage
1%	20	18 sec	51 sec
2%	40	38 sec	2 min 33 sec
5%	100	1 min 35 sec	11 min 14 sec
10%	200	3 min 36 sec	74 min 25 sec

Table 7.3: The comparison of the computation speed of Cross-correlation and Montage registration techniques

Chapter 8

Conclusion and further improvements

The intention of this work was the implementation of the Lucky Imaging technique, which consist of two separate parts: measuring focus of short-exposed digital astronomical pictures and registration of those well-focused images.

The main goals of the thesis were fulfilled: a review of usable focus measures and registration techniques has been done and a software based on these algorithms has been produced. However, due to lack of real data only limited testing has been done. Nevertheless, the results show, that the algorithms work well and mostly do satisfy the imposed requirements. Unfortunately, no practical results have been achieved, i.e. the angular resolution of the single target processed (the star ζ -Bootis) could not have been improved, as the used telescope has a too low pixelscale and therefore strongly undersamples the target.

In order to improve the software performance, first and foremost more data must be processed in the future, to tune-out the algorithms (in particular star segmentation) and explore their stability with respect to blur and noise. With the used telescope of unchanged pixelscale and FWHM, visible angular resolution improvement can only be achieved for objects at least 2.7 arc seconds apart, as they should cover at least an area of 4x4 pixels on the digital image.

Appendix A

The LI-software

The produced software is a combination of C-language binaries, bash- and MATLAB[®]-scripts, making use of foreign software packages Montage and Eclipse. It was developed and tested under the Ubuntu Linux operating system.

A.1 User documentation

The user uses the software via several bash-commands, divided into two groups. The first group of commands serves to run the whole LI-process on large datasets:

```
$ li-stars <p>
```

This command performs LI (strehl-montage) on <p>% of best images of stars, paths to images on standard input.

```
$ li-planets [-m {glv|wavelet|moments}] [-r {CC|Montage}] <p>
```

This command performs LI on <p>% of best planetary images, paths to images on standard input. Option `-m` sets the focus-measure (the default is “glv”). Option `-r` sets the registration method (the default is “Montage”).

A typical use may therefore be:

```
$ ls /images/saturn/* | li-planets 10
```

Prints out the name of the produced file:

```
LI010.fits
```

The second group of commands serves for measuring focus of individual images for user-testing purposes. The commands are:

```
$ focus-measure-strehl FILE_1.fits FILE_2.fits ...
$ focus-measure-glv FILE_1.fits FILE_2.fits ...
$ focus-measure-moments FILE_1.fits FILE_2.fits ...
$ focus-measure-wavelet FILE_1.fits FILE_2.fits ...
```

The commands print out for each input file its name and its focus-measure value, separated by a colon.

A typical use may be:

```
$ focus-measure-glv fits/planets/nowcs/saturn-05_08/*
```

Prints out:

```
fits/planets/nowcs/saturn-05_08/20070508220248-0775-RA.fits: 59457
fits/planets/nowcs/saturn-05_08/20070508220547-0838-RA.fits: 59146
fits/planets/nowcs/saturn-05_08/20070508220846-0597-RA.fits: 56771
...
```

A.2 CD content

The attached CD contains following items:

- `eclipse/eclipse.zip` – the revised and adopted Eclipse framework
- `output_fits/` – directory containing the output of the software: 1%, 2%, 5% and 10% selections of the star ζ -Bootis and the planet Saturn, registration by CC and Montage
- `prog/bash/` – bash scripts
- `prog/bin/` – C-language binaries
- `prog/octave/` – MATLAB[®]-scripts (wavelet and moments focus measures)
- `prog/src/` – the source files written in C language
- `prog/li-config` – a configuration utility for easy installation
- `test_fits/` – directory contains examples of processed data: the star ζ -Bootis and the planet Saturn, with and without WCS information
- `thesis.pdf` – the online version of this document
- `INSTALL` – installation instructions
- `README` – notes on how to use the software

Appendix B

Used telescope, CCD and software environment

This appendix contains technical information about devices and software used to acquire processed data.

B.1 RTS2

RTS2 (Remote Telescope System 2nd Version) is a software package designed for full automatization of astronomical observations. The system automatizes whole process from the target selection from a database until the processing of acquired images. Today, five telescopes on three continents are controlled by this system.

RTS2 was originally proposed for controlling telescopes devoted to observation of optical opposites of gamma-bursts. During development, it became a general system for controlling robotic telescopes.

For further information, see [24].

B.2 Bootes-IR

Bootes-IR is a Spanish(IAA-CSIC, Granada)-Czech(AsÚ AV ČR Ondřejov) telescope located at the OSN (Observatory de Sierra Nevada) in the Sierra Nevada mountains, near IAA, Granada, 2890 m above sea level. The Ritchie-Crétien telescope made by the German company ASTELCO is mounted on a full robotic ASTELCO/Tau-Tec mounting. Primary mirror is 60 cm in diameter, secondary mirror 10 cm in diameter. The pixelscale is 0.69 arc seconds per pixel, average FWHM is 3 pixels.

The telescope is equipped with an Andor Technologies optic camera with the DV-887 head. The camera uses a EMCCD (<http://www.emccd.com>) chip of 512x512 pixels. The focusation is via shifting the secondary mirror. The

telescope uses a FLI (Finger Lake Instruments) filter-wheel with UBVRIZ filters.

For further information, see [25].

B.3 Watcher

Watcher is an Irish robotic telescope with, with Czech (AsÚ AV ĀR Ondřejov), Spanish (IAA-CSIC, Granada) and South-African (Boyden observatory, University of Bloemfontein) participation. It is located at Boyden Observatory near the Bloemfontein city in Republic of South Africa. The telescope is operated by the Irish UCD (University College Dublin).

The telescope is of the Cassergrain type, it's primary mirror is 40 cm in diameter, the secondary mirror is 4 cm in diameter. The pixelscale is 0.84 arc seconds per pixel, average FWHM is 2.5 pixels.

The telescope is located on a Software Bisquit Paramount robotic mounting, equipped with a Apogee camera with Kodak KAF 1001e of 1024x1024 pixels and a Optec filter-wheel with standard science-grade BVRI filters.

For further information, see [26].

Bibliography

- [1] Saint-Pé O. et al.: Demonstration of Adaptive Optics for Resolved Imaging of Solar System Objects, 1993, *Icarus*, 105, 263
- [2] Lloyd-Hart M. et al.: Adaptive optics for the 6.5 m MMT, 2000, <http://athene.as.arizona.edu/lclose/AOPRESS/>
- [3] R. Kašpar: Reducing noise in IR images, Diploma thesis, Faculty of Mathematics and Physics, Charles University in Prague, 2002
- [4] N. M. Law et al.: Lucky imaging: high angular resolution imaging in the visible from the ground 2006, *A&A*, 446, 739
- [5] Homepage of the Lucky Imaging Team at Cambridge University: http://www.ast.cam.ac.uk/optics/Lucky_Web_Site/
- [6] B. Jähne: Digital Image Processing, 2005, Springer Verlag
- [7] Boyle, W.S.; Smith, G.E.: The inception of charge-coupled devices, *Electron Devices*, IEEE Transactions on Volume 23, Issue 7, Jul 1976 Page(s): 661 - 663
- [8] Andor technology: Digital Cameras – Camera Sensitivity and Noise. http://www.andor.com/library/digital_cameras/
- [9] Möller, K. D.: Optics: learning by computing with examples using MathCAD, 2003 Springer-Verlag New York
- [10] W. Huang, Z. Jing: Evaluation of focus measures in multi-focus image fusion, *Elsevier* 28, pages 493 - 500, 2007
- [11] M. Subbarao et al.: Focusing techniques, Stony Brook, New York, 1992
- [12] J. Flusser et al.: A new wavelet-based measure of image focus, *Elsevier* 23, pages 1785-1794, 2002
- [13] Y. Zhang, Y. Zhang, C. Wen: A new focus measure using moments, *Elsevier* 18, pages 959 - 969, 2000

- [14] J. Flusser et al.: Moments and moment invariants in image analysis, A tutorial proposal. <http://staff.utia.cas.cz/zitova/tutorial/index.html>
- [15] R. Gonzales, R. Woods: Digital Image Processing, 2002, Prentice Hall
- [16] I. Kaplan: The Daubechies D4 Wavelet Transform, 2002: www.bearcave.com/misl/misl_tech/wavelets/daubechies/index.html
- [17] Dr. Karl Strehl - Fränkischer Gelehrter, Physiker und Optiker von Weltruf, <http://www.kurt-hopf.de/astro/strehl.htm>
- [18] C. Perrier: Amplitude estimation from speckle interferometry, NATO ASI Series C, Vol. 274, 1989
- [19] ECLIPSE – ESO C Library for an Image Processing Software Environment, European Southern Observatory, 2005, <http://www.eso.org/projects/aot/eclipse/>
- [20] J. Flusser, B. Zittová: Image registration methods: a survey, Elsevier 21, pages 977-1000, 2003
- [21] E.W.Greisen, M.R. Calabretta - Representations of world coordinates in FITS, A & A 395, pages 1061 - 1075, 2002
- [22] Equatorial Coordinates: <http://www.astronomy.org/astronomy-survival/coord.html>
- [23] Montage: An Astronomical Image Mosaic System: <http://montage.ipac.caltech.edu/>
- [24] Kubánek, P., Jelínek, M., Vítek, S., de Ugarte Postigo, A., Nekola, M., & French, J.: RTS2: a powerful robotic observatory manager, 2006, SPIE, 6274,
- [25] Castro-Tirado, A. J., et al.:BOOTES-IR: a robotic nIR astronomical observatory devoted to follow-up of transient phenomena, 2006, SPIE, 6267,
- [26] French, J., et al.: Watcher: A Telescope for Rapid Gamma-Ray Burst Follow-Up Observations, 2004, Gamma-Ray Bursts: 30 Years of Discovery, 727, 741
- [27] Möller, K. D.: Optics: learning by computing with examples, page 147
- [28] <http://mathworld.wolfram.com/GnomonicProjection.html>
- [29] <http://www.astro.uiuc.edu/kaler/sow/zetaboo.html>

- [30] http://en.wikipedia.org/wiki/Astronomical_seeing
- [31] <http://www.answers.com/topic/adaptive-optics>
- [32] <http://en.wikipedia.org/wiki/Fwhm>
- [33] <http://montage.ipac.caltech.edu/docs/algorithms.html>